Supplementary Information

# Exploration of organic superionic glassy conductors by process and materials informatics with lossless graph database

Kan Hatakeyama-Sato,[a)*] Momoka Umeki,[a)] Hiroki Adachi,[a)]

Naoaki Kuwata,[b)] Gen Hasegawa,[b)] Kenichi Oyaizu[a)*]

[a)] Department of Applied Chemistry, Waseda University, 3-4-1 Okubo, Shinjuku, Tokyo 169-8555, Japan

b) National Institute for Materials Science (NIMS), 1-1 Namiki, Tsukuba 305-0044, Japan

# Supplementary Figures, Tables, and Discussions

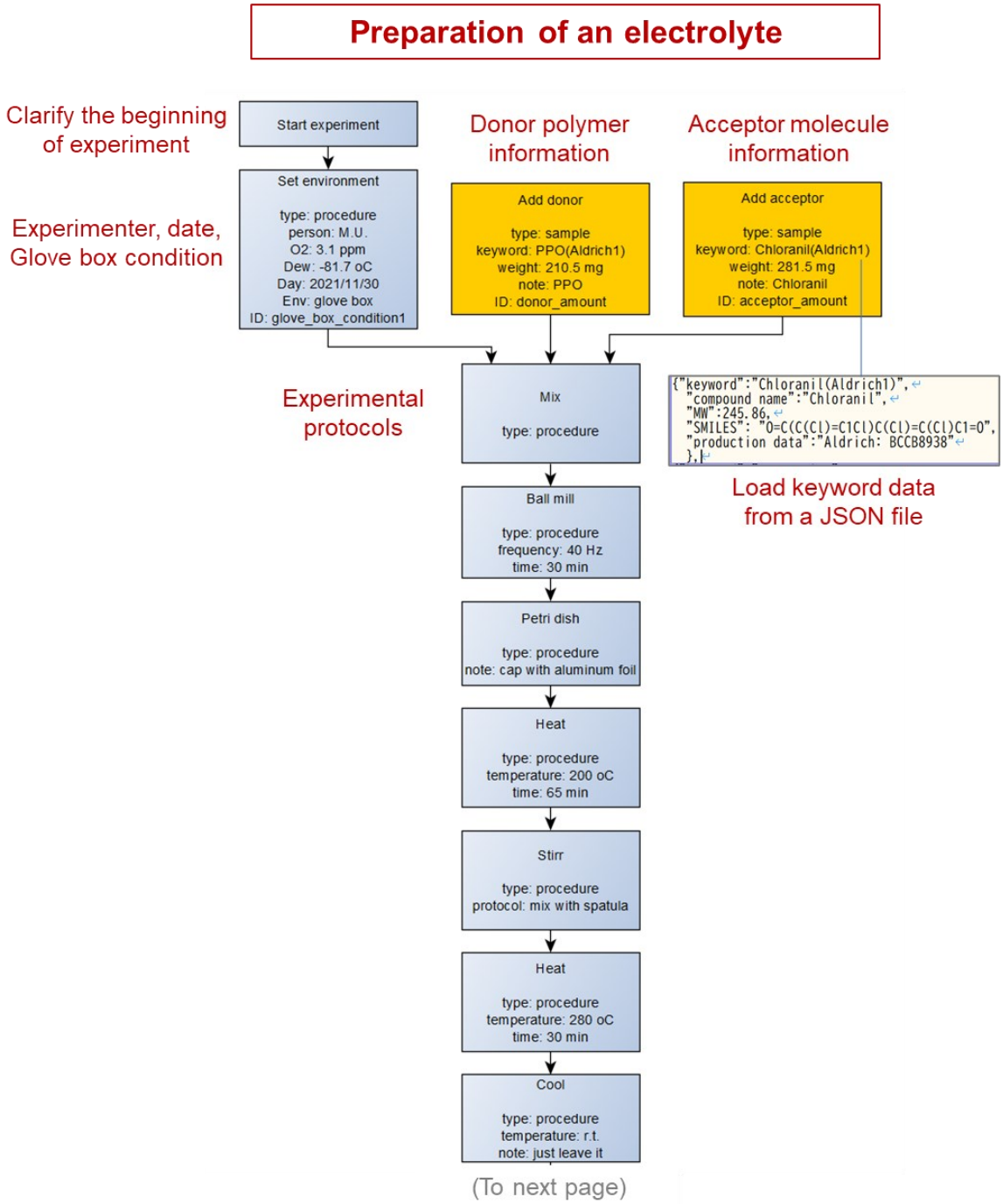

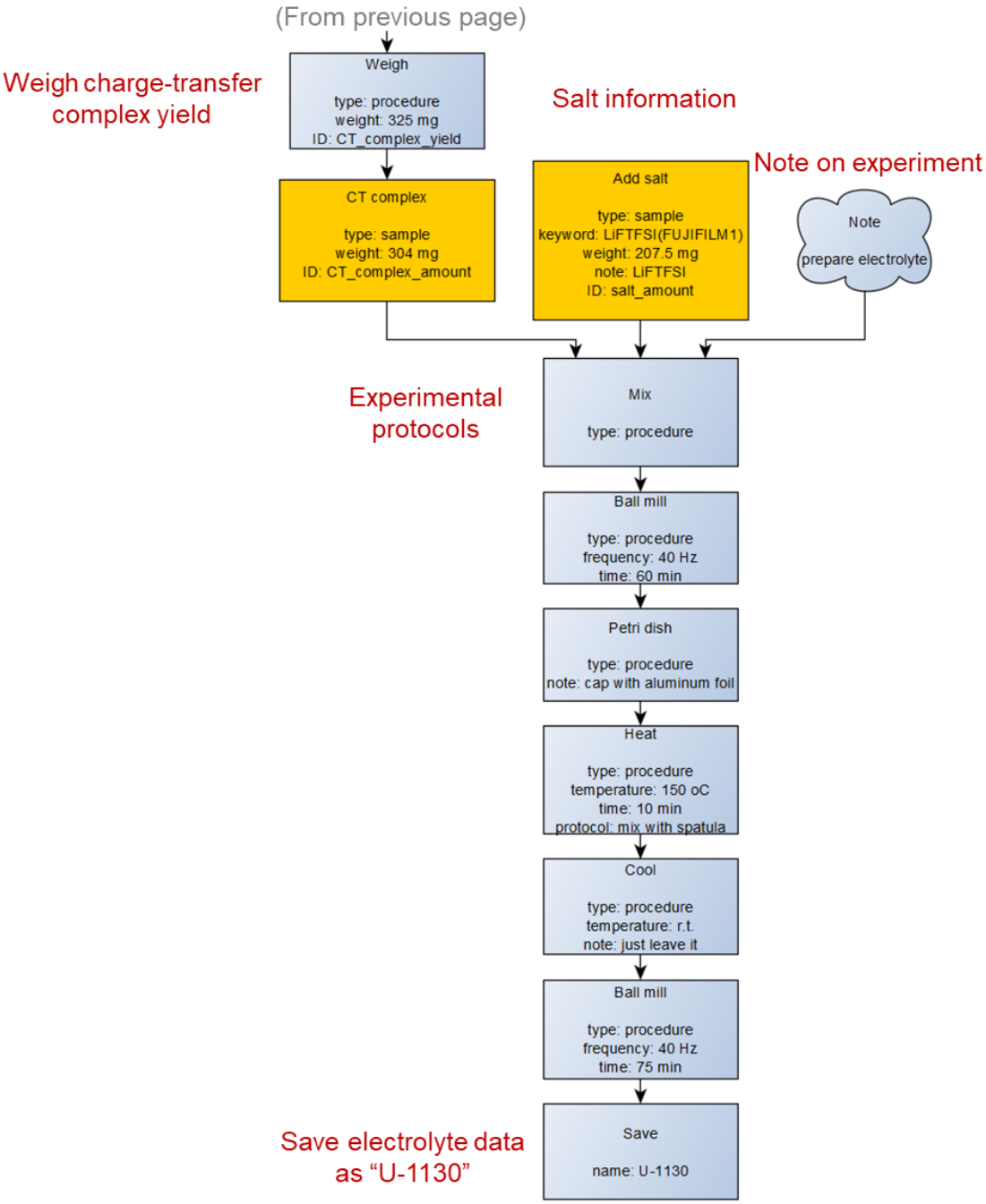
(From previous page)
Weigh charge-transfer complex yield
Weigh
type: procedure
weight: 325 mg
ID: CT_complex_yield
Salt information
Note on experiment
CT complex
type: sample
weight: 304 mg
ID: CT_complex_amount
Add salt
type: sample
keyword: LiFTFSI(FUJIFILM1)
weight: 207.5 mg
note: LiFTFSI
ID: salt_amount
Note
prepare electrolyte
Experimental protocols
Mix
type: procedure
Ball mill
type: procedure
frequency: 40 Hz
time: 60 min
Petri dish
type: procedure
note: cap with aluminum foil
Heat
type: procedure
temperature: 150 oC
time: 10 min
protocol: mix with spatula
Cool
type: procedure
temperature: r.t.
note: just leave it
Ball mill
type: procedure
frequency: 40 Hz
time: 75 min
Save electrolyte data as “U-1130”
Save
name: U-1130

a)

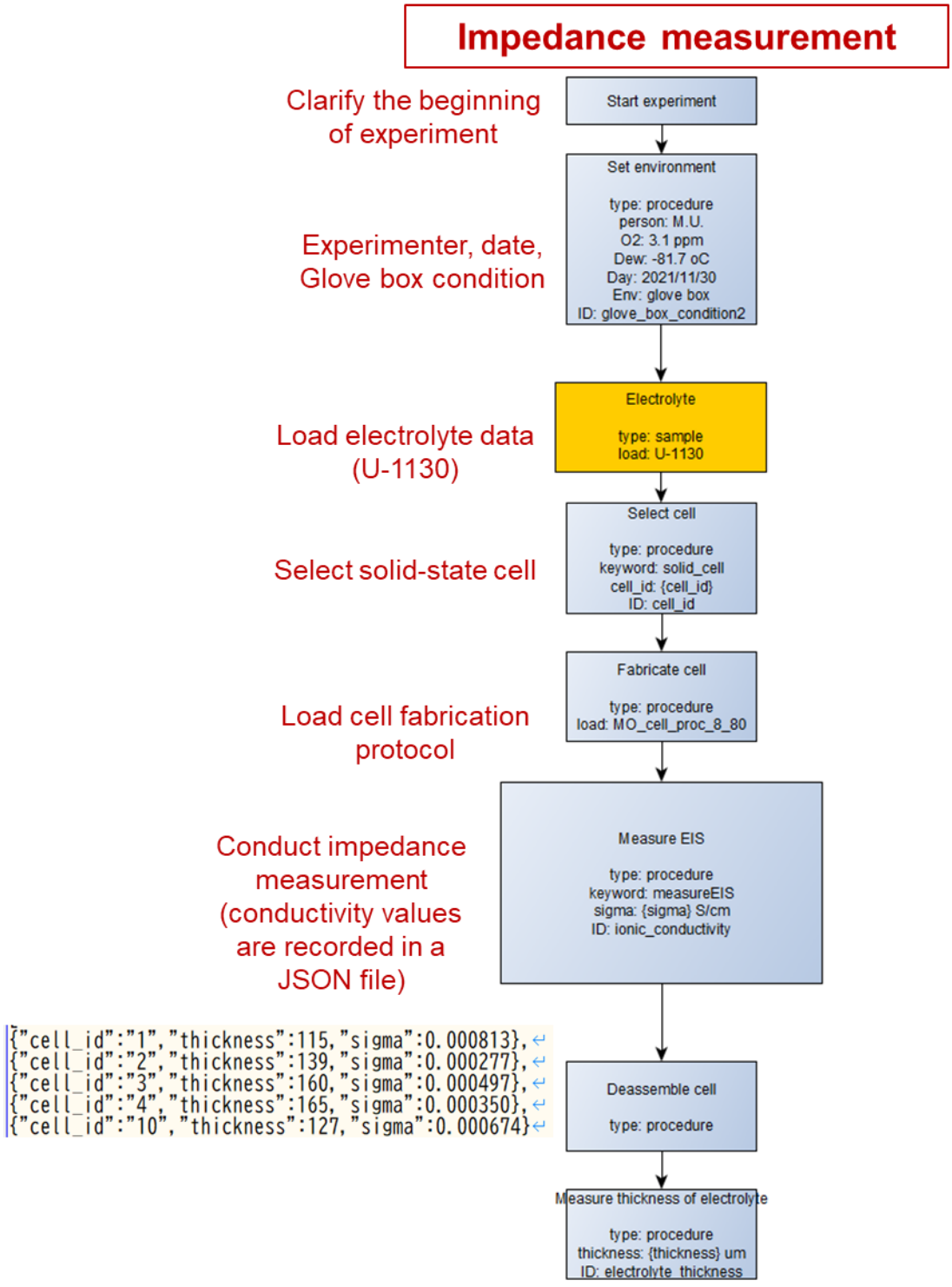
Impedance measurement
Clarify the beginning of experiment
Start experiment
Set environment
type: procedure
person: M.U.
O2: 3.1 ppm
Dew: -81.7 oC
Day: 2021/11/30
Env: glove box
ID: glove_box_condition2
Experimenter, date, Glove box condition
Electrolyte
type: sample
load: U-1130
Load electrolyte data (U-1130)
Select cell
type: procedure
keyword: solid_cell
cell_id: {cell_id}
ID: cell_id
Select solid-state cell
Fabricate cell
type: procedure
load: MO_cell_proc_8_80
Load cell fabrication protocol
Measure EIS
type: procedure
keyword: measureEIS
sigma: {sigma} S/cm
ID: ionic_conductivity
Conduct impedance measurement (conductivity values are recorded in a JSON file)
{"cell_id":"1","thickness":115,"sigma":0.000813},
{"cell_id":"2","thickness":139,"sigma":0.000277},
{"cell_id":"3","thickness":160,"sigma":0.000497},
{"cell_id":"4","thickness":165,"sigma":0.000350},
{"cell_id":"10","thickness":127,"sigma":0.000674}
Deassemble cell
type: procedure
Measure thickness of electrolyte
type: procedure
thickness: {thickness} um
ID: electrolyte_thickness

b)

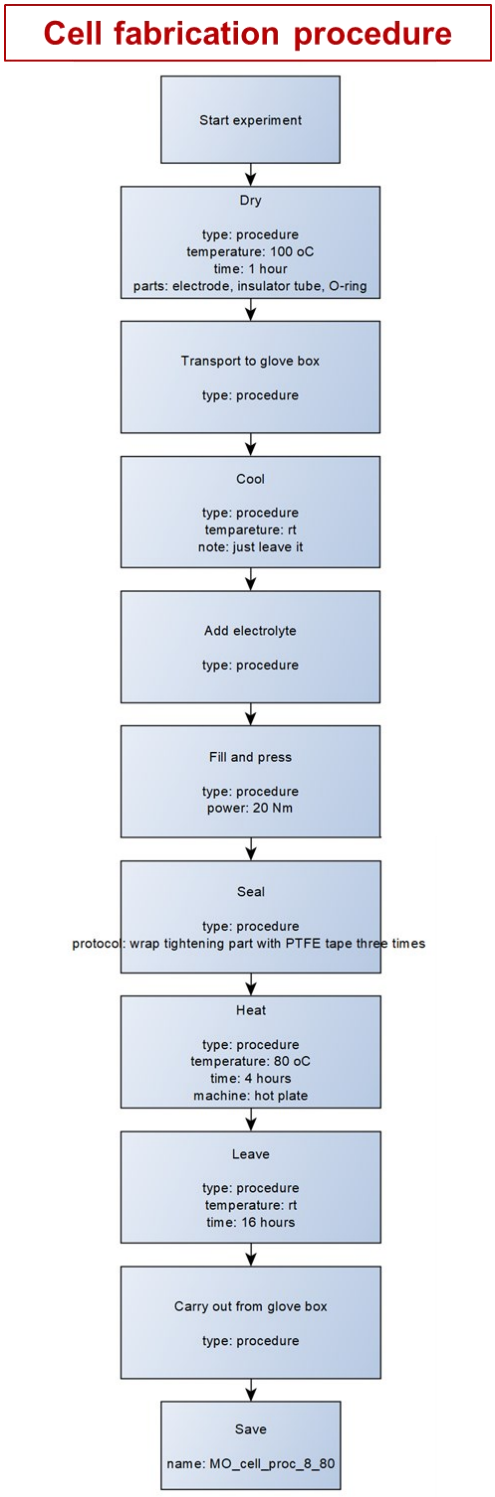


c)

**Supplementary Figure 1 | Examples of graph-shaped data, describing experimental procedures.** **a,** Electrolyte preparation. **b,** Impedance measurement. **c,** Cell fabrication. Corresponding graphml files are available from the public repository.

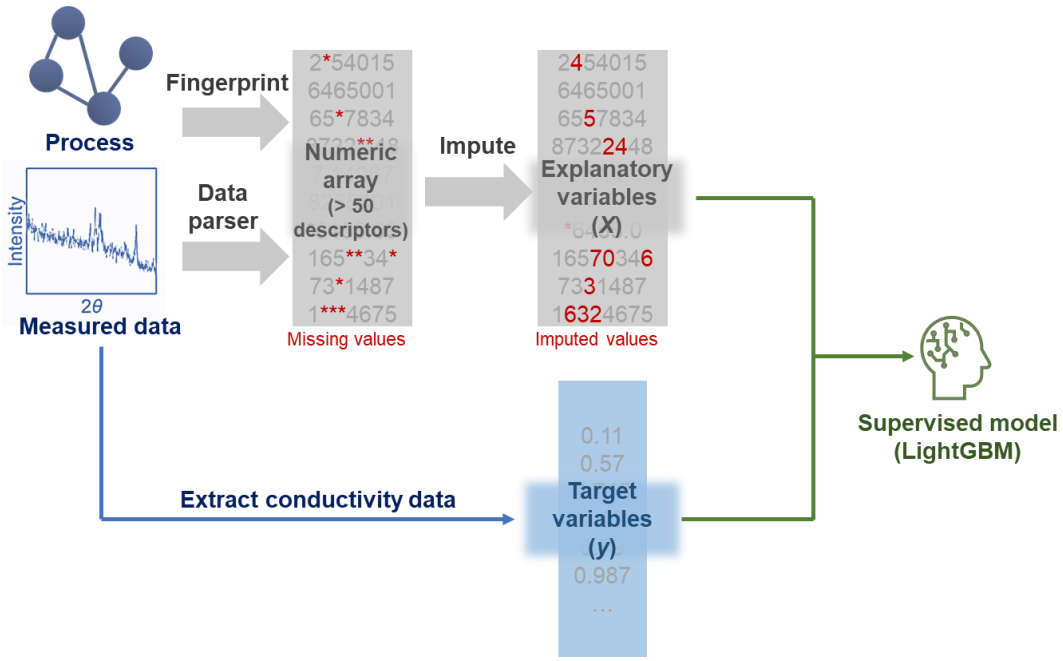


**Supplementary Figure 2 | Flow of processing graph and measurement data for machine learning.** Graph-shaped experimental data are conventional into a numeric array by a fingerprint algorithm. Characteristic numeric information is extracted from measurement data. Then, missing values in the numeric array are imputed by machine learning. Finally, the relationship between the imputed data and target variables (ionic conductivity) is studied by a supervised model.

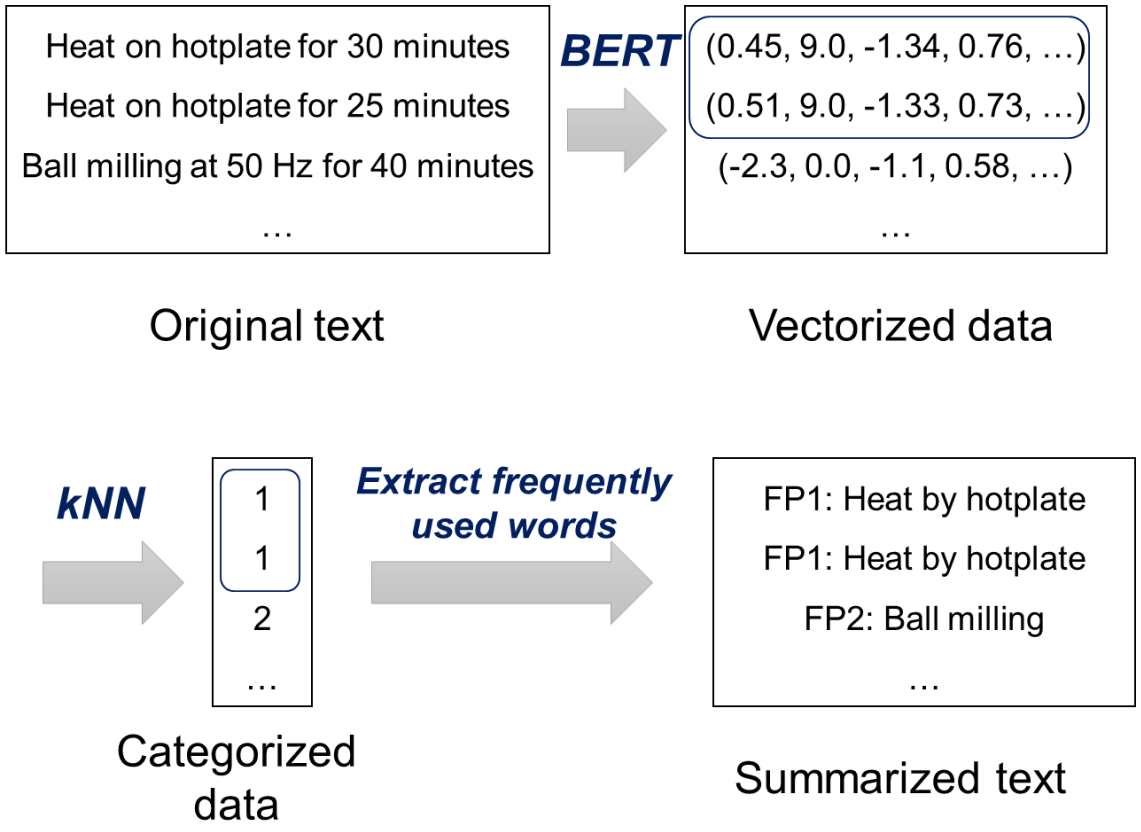


**Supplementary Figure 3 | Scheme for processing fingerprints.** First, original experimental text was collected from the graph nodes. The text was vectorized by BERT and grouped by a *k*NN model. Frequently used words were extracted to express each fingerprint (FP1, FP2, …).

**Supplementary Table 1. Representative process fingerprints and their meanings.[a]**

| ID | Fingerprint [b] | Typical meaning |
|---|---|---|
| **1** | temperature-Heat-mix-with-spatula\|Petri-dish-Cool-Heat-Refill | Heat the sample and mix with a spatula. Then, cool or heat it. |
| **2** | Heat-temperature-300°C-30min-160°C\|Heat-Cool-Petri-dish- | Heat the sample at typical temperatures of 300 or 160°C for 30 min. Then, cool it. |
| **3** | Heat-temperature-200°C-30min-20min\|Petri-dish-Heat-Stirr- | Heat the sample at a typical temperature of 200°C for 20 or 30 min. Then, heat it. |
| **4** | Ball-mill-frequency-50Hz-30min\|CT-complex-Measure-particle-size | Ball mill the sample with a typical frequency of 50 Hz for 30 min. Then, measure particle size. |
| **5** | sample-temperature-CT-complex-Seal\|Heat-Fill-Ball-mill-and | Prepare a charge-transfer complex and conduct additional steps (e.g., sealing, heating, and ball milling). |
| **6** | Ball-mill-frequency-50Hz-60min\|Cool-Select-cell-Fill-sample | After cooling, ball mill the sample with a typical frequency of 50 Hz for 60 min. Then, fill a cell with it. |
| **7** | Weigh-Set-environment-\|Ball-mill-Set-environment-Fill | Weigh sample, ball milling, etc. |
| **8** | sample-Carry-out-from-glove\|Ball-mill-Weigh-Seal-Measure | Remove a cell from a glove box. Then, measure it. |
| **9** | temperature-Measure-machine-AMF-20N-EIS\|Break-vacuum-pack-Carry-out | Anneal a cell in an incubator (AMF-20N) and open a vacuum pack before measurement. |
| **10** | Ball-mill-frequency-50Hz-60min\|Cool-Grind-Ball-mill-Wash | Ball mill the sample with a typical frequency of 50 Hz for 60 min. Then, conduct additional steps (e.g., cooling, grinding, and ball milling). |
| **11** | temperature-machine-AMF-20N-Measure-EIS\|Carry-out-from-glove-box | Remove a cell from a glove box and anneal it an incubator (AMF-20N). |
| **12** | sample-Fill-fill-into-Disassemble\|Cool-Carry-out-from-glove | Fill an NMR tube with a sample and remove it from the glove box. |
| **13** | Ball-mill-frequency-50Hz-30min\|Mix-Petri-dish-Cool-Carry | Ball mill the sample with a typical frequency of 50 Hz for 30 min. Then, conduct some additional steps |
| **14** | Fill-sample-fill-into-tube\|Carry-out-from-glove-box | Fill an NMR tube with a sample and remove it from the glove box. |
| **15** | Measure-Carry-out-from-glove\|Seal-Ball-mill-Fill-sample | Remove the sample from the glove box, followed by filling and sealing a cell. |
| **16** | temperature-Leave-rt-Seal-wrap\|Seal-glove-box-Carry-out | After sealing, keep the cell in a glove box for some time before removing it. |
| **17** | Ball-mill-frequency-50Hz-15min\|Ball-mill-Select-cell-Fill | Ball mill the sample with a typical frequency of 50 Hz for 15 min. Then, conduct some additional steps |
| **18** | Break-vacuum-pack-Transport-to\|Leave-Cool-Dry-Measure-EIS | Open vacuum pack containing a cell, and measure impedance. |
| **19** | Add-Cool-anode-cathode-electrolyte\|Add-electrolyte-Transport-to-glove | Add cathode, anode, and electrolyte to fabricate a cell. |
| **20** | Seal-Measure-EIS-vacuum-pack\|Carry-out-from-glove-box | Seal a cell in a vacuum pack and remove it from the glove box. |

[a] Full data are available in Supplementary Data. [b] The original fingerprints were automatically grouped by BERT and *k*NN models, and frequently used words were extracted. Expression of 'AAA|BBB' indicates that a representative step 'AAA' neighbours 'BBB'.

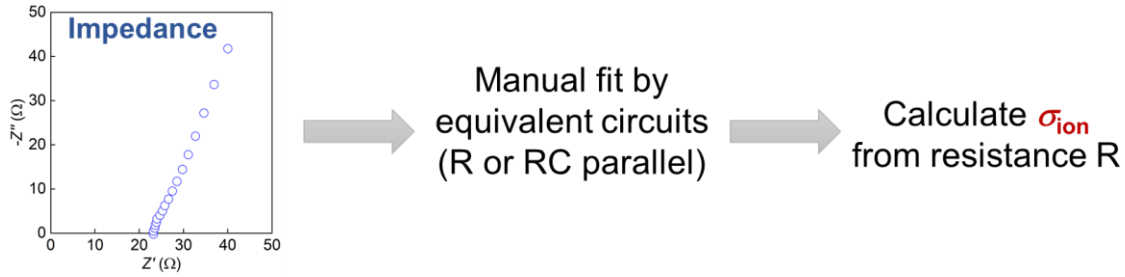
Impedance
-Z'' (Ω)
Z' (Ω)
Manual fit by equivalent circuits (R or RC parallel)
Calculate $\sigma_{ion}$ from resistance R

a)

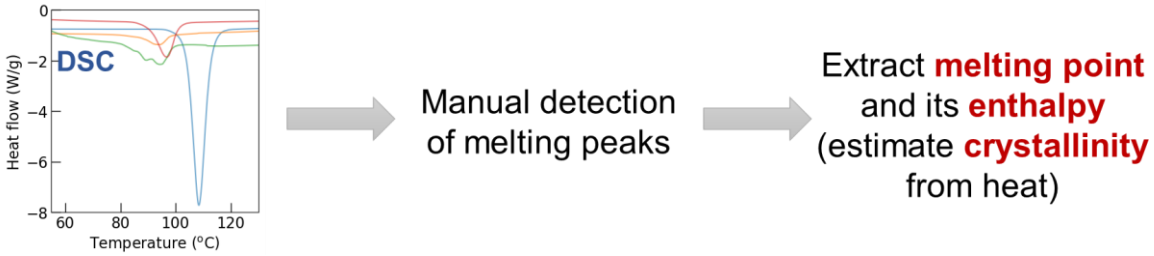
DSC
Heat flow (W/g)
Temperature (°C)
Manual detection of melting peaks
Extract melting point and its enthalpy (estimate crystallinity from heat)

b)

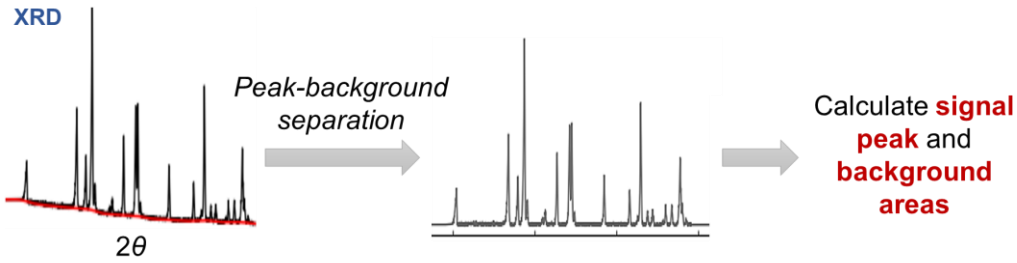
XRD
2θ
Peak-background separation
Calculate signal peak and background areas

c)

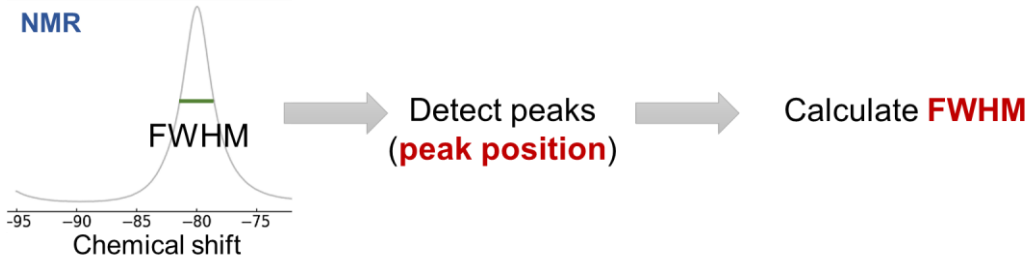
NMR
FWHM
Chemical shift
Detect peaks (peak position)
Calculate FWHM

d)

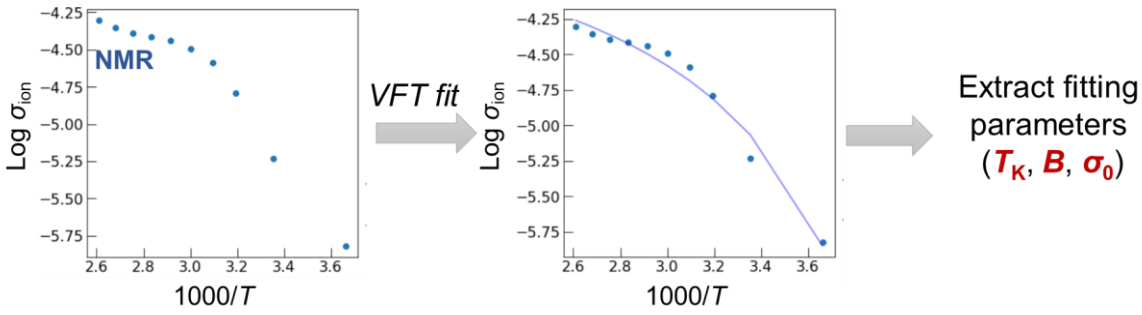
NMR
Log $\sigma_{ion}$
1000/T
VFT fit
Extract fitting parameters ($T_K$, $B$, $\sigma_0$)

e)

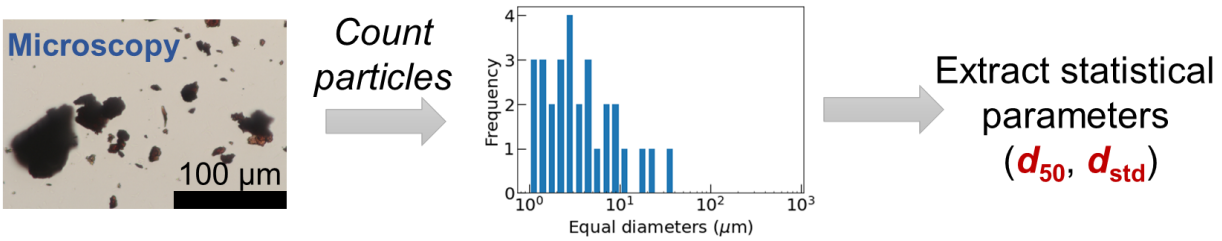


f)

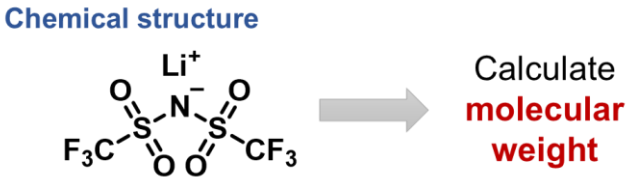


g)

**Supplementary Figure 4 | Schemes to extract descriptors from experimental data. a,** Impedance spectrum. **b,** DSC. **c,** XRD. **d,** Solid-state $^{7}$Li and $^{19}$F NMR. **e,** Temperature dependence of conductivity. **f,** Particle size. **g,** Chemical structures.

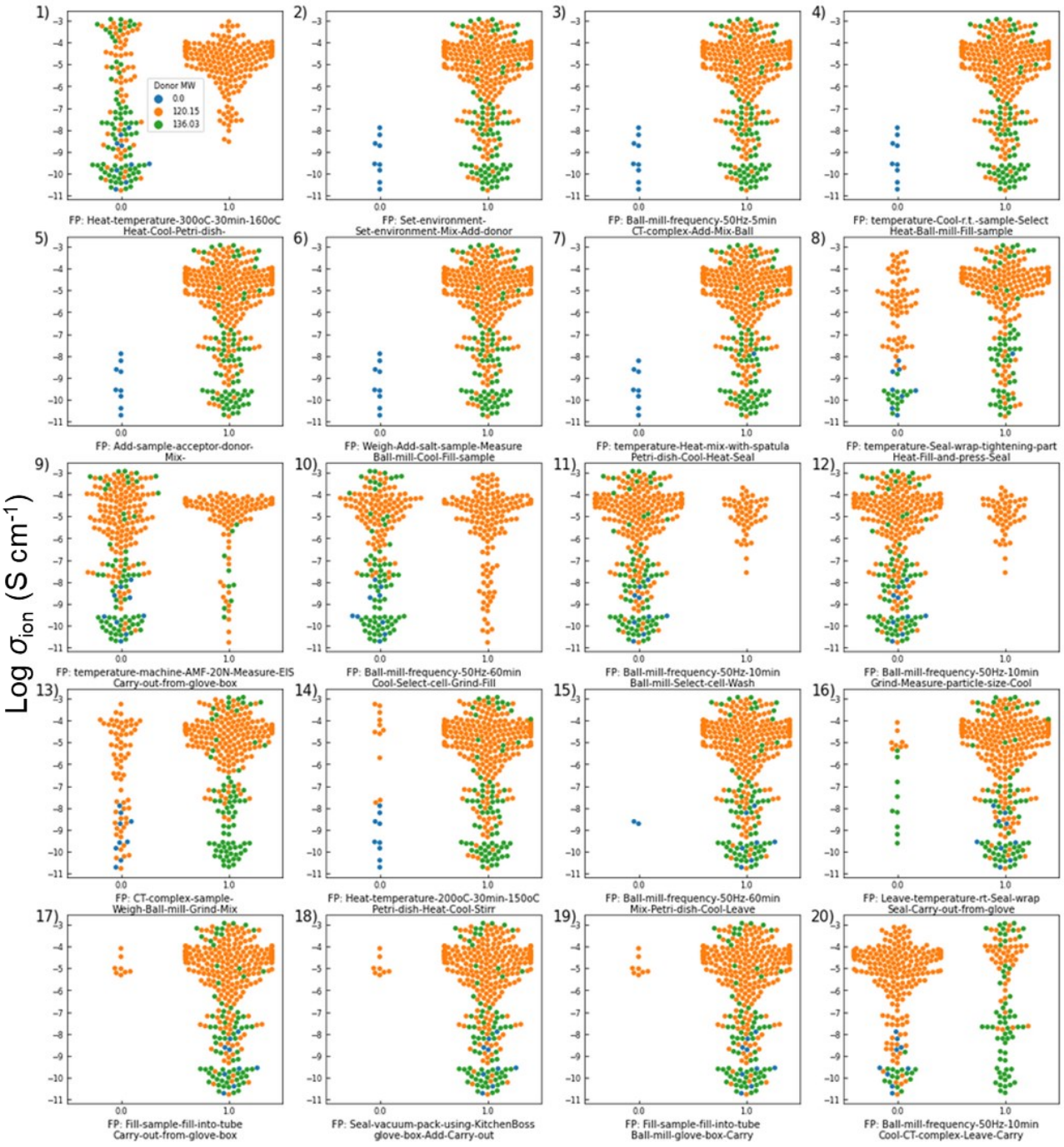


**Supplementary Figure 5 | Relationships between conductivity and primary fingerprints of experimental steps.**

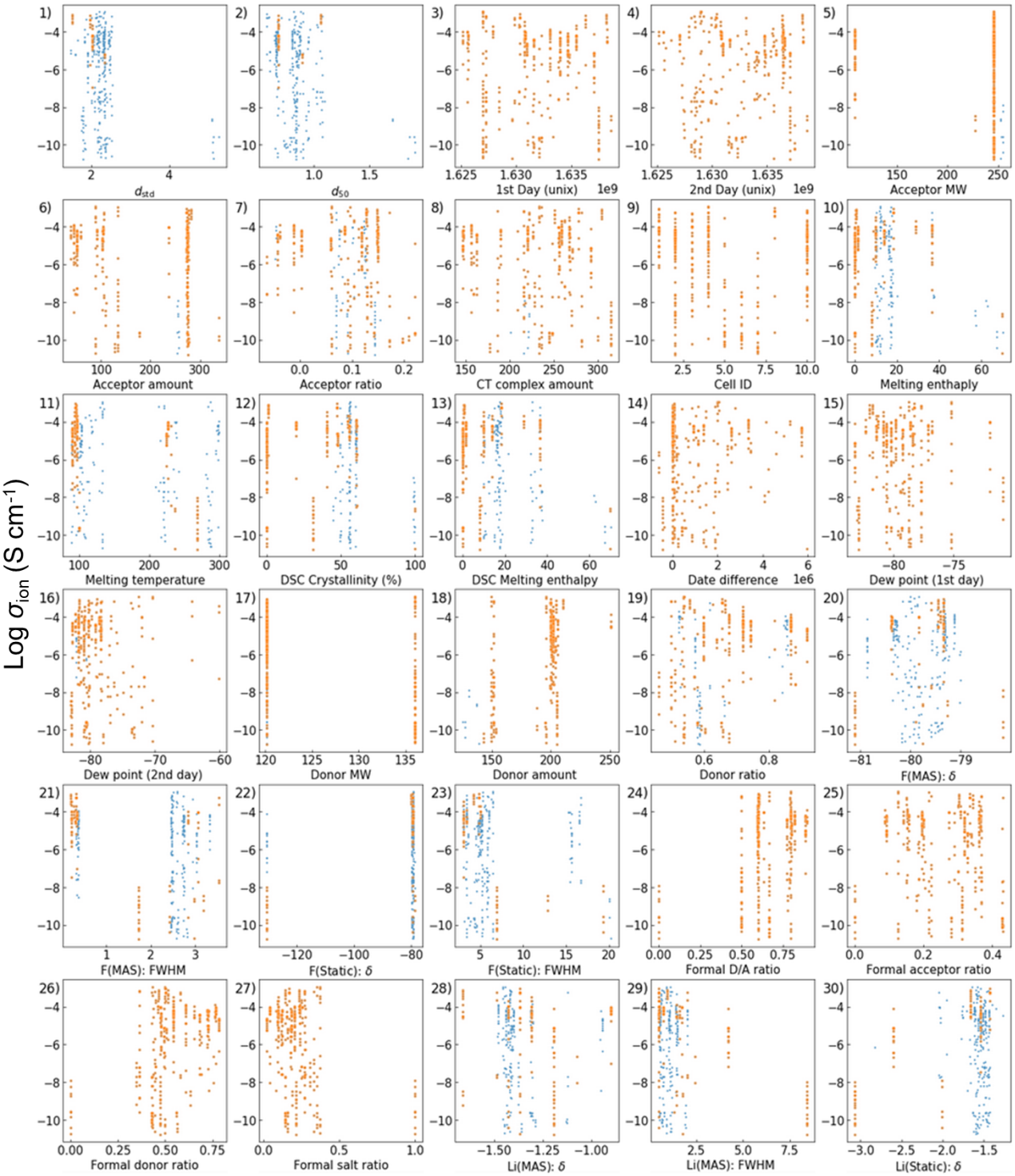
Log $\sigma_{ion}$ (S cm$^{-1}$)
1) $d_{std}$
2) $d_{50}$
3) 1st Day (unix) 1e9
4) 2nd Day (unix) 1e9
5) Acceptor MW
6) Acceptor amount
7) Acceptor ratio
8) CT complex amount
9) Cell ID
10) Melting enthaply
11) Melting temperature
12) DSC Crystallinity (%)
13) DSC Melting enthalpy
14) Date difference 1e6
15) Dew point (1st day)
16) Dew point (2nd day)
17) Donor MW
18) Donor amount
19) Donor ratio
20) F(MAS): $\delta$
21) F(MAS): FWHM
22) F(Static): $\delta$
23) F(Static): FWHM
24) Formal D/A ratio
25) Formal acceptor ratio
26) Formal donor ratio
27) Formal salt ratio
28) Li(MAS): $\delta$
29) Li(MAS): FWHM
30) Li(Static): $\delta$

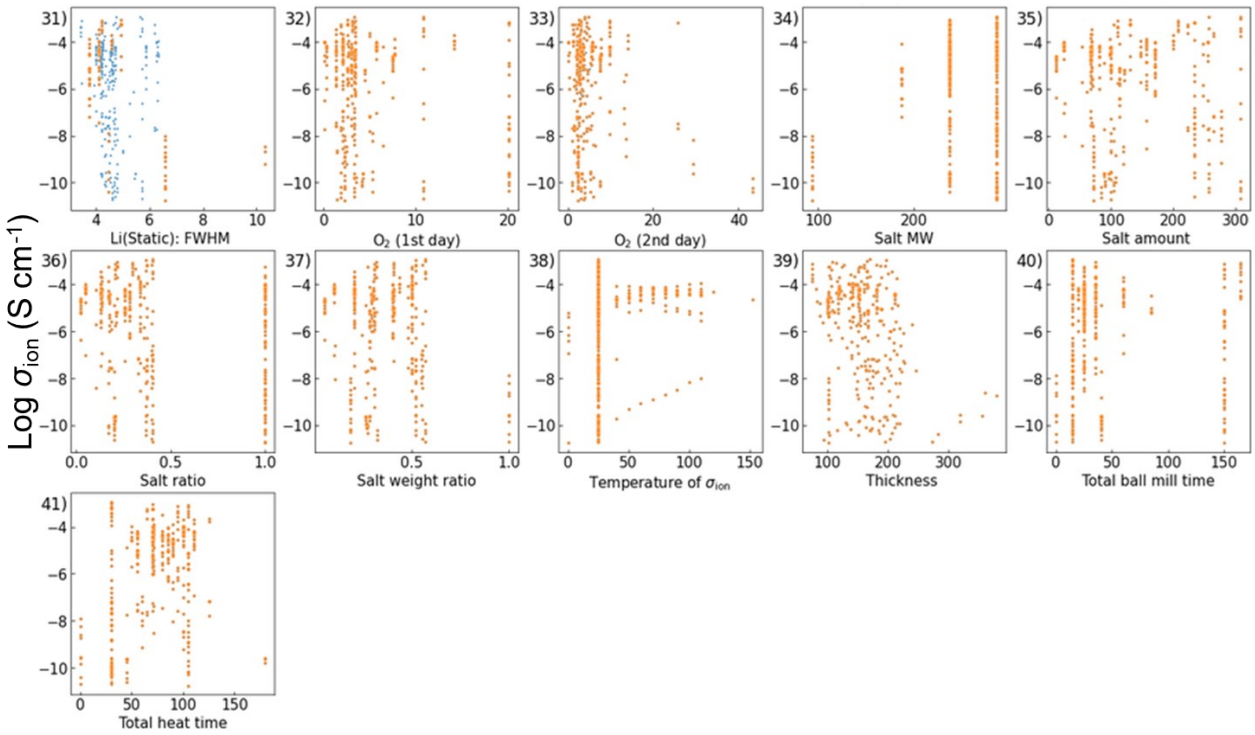


**Supplementary Figure 6 | Relationships between conductivity and experimental descriptors (excluding fingerprint).** Blue plots show values imputed by a machine learning model.

**Supplementary Table 2. Major parameters for analyzing electrolytes.**

| Parameter | Unit | Explanation |
|---|---|---|
| $d_{std}$ | μm | Standard deviation of particle diameters (estimated by optical microscopy) |
| $d_{50}$ | μm | Median of particle diameters (estimated by optical microscopy) |
| 1st day (Unix) | - | Date of electrolyte preparation (Unix time) |
| 2nd day (Unix) | - | Date of cell fabrication for impedance measurement (Unix time) |
| Acceptor MW | - | The molecular weight of the acceptor molecule |
| Acceptor amount | mg | Actual amount of acceptor forming a charge-transfer complex |
| Acceptor ratio | - | Estimated molar ratio of acceptor in an electrolyte, considering acceptor sublimation |
| CT complex amount | mg | Actual amount of charge-transfer complex mixed with the salt |
| Cell ID | - | Solid-state cell equipment ID, which was uniquely numbered in the project (same model number) |
| DSC melting temperature | °C | Melting temperature of salt estimated by DSC |
| DSC crystallinity | % | Estimated crystallinity of salt, calculated from melting enthalpy (assuming pristine salt exhibited 100% crystallinity) |
| DSC melting enthalpy | J $g^{-1}$ | Melting enthalpy of salt estimated by DSC |
| Date difference | - | Second day (Unix) minus first day (Unix) |
| Dew point (1st day) | °C | Dew point in the glove box during electrolyte preparation |
| Dew point (2nd day) | °C | Dew point in the glove box during cell fabrication |
| Donor MW | - | Molecular weight of the donor molecule (polymer) |
| Donor amount | mg | Actual amount of a donor forming the charge-transfer complex |
| Donor ratio | - | Estimated molar ratio of a donor in an electrolyte, considering acceptor sublimation |
| F (MAS): $\delta$ | ppm | Chemical shift of $^{19}F$ peak during solid-state MAS NMR |
| F (MAS): FWHM | ppm | FWHM of $^{19}F$ peak during solid-state MAS NMR |
| F (static): $\delta$ | ppm | Chemical shift of $^{19}F$ peak during solid-state static NMR |
| F (static): FWHM | ppm | FWHM of $^{19}F$ peak during solid-state static NMR |
| Formal donor/acceptor ratio | - | Molar ratio of donor and acceptor molecules, ignoring acceptor sublimation |
| Formal acceptor ratio | - | Estimated molar ratio of a donor in an electrolyte, ignoring acceptor sublimation |
| Formal donor ratio | - | Estimated molar ratio of a donor in an electrolyte, ignoring acceptor sublimation |
| Formal salt ratio | - | Estimated molar ratio of salt in an electrolyte, ignoring acceptor sublimation |
| Li (MAS): $\delta$ | ppm | Chemical shift of $^{7}Li$ peak during solid-state MAS NMR |
| Li (MAS): FWHM | ppm | FWHM of $^{7}Li$ peak during solid-state MAS NMR |
| Li (static): $\delta$ | ppm | Chemical shift of $^{7}Li$ peak during solid-state static NMR |
| Li (static): FWHM | ppm | FWHM of $^{7}Li$ peak during solid-state static NMR |

| | | |
|---|---|---|
| $O_2$ (1st day) | ppm | $O_2$ concentration in the glove box during electrolyte preparation |
| $O_2$ (2nd day) | ppm | $O_2$ concentration in the glove box during cell fabrication |
| Salt MW | - | Molecular weight of the salt molecule |
| Salt amount | mg | Actual amount of salt forming a charge-transfer complex |
| Salt ratio | - | Estimated molar ratio of salt in an electrolyte, considering acceptor sublimation |
| Salt weight ratio | - | Actual weight ratio of salt in the electrolyte |
| Temperature of $\sigma_{ion}$ | °C | Measurement temperature of $\sigma_{ion}$ |
| Thickness | μm | Electrolyte thickness |
| Total ball milling time | min | Total ball milling time to prepare the electrolyte |
| Total heating time | min | Total heating time to prepare the electrolyte |

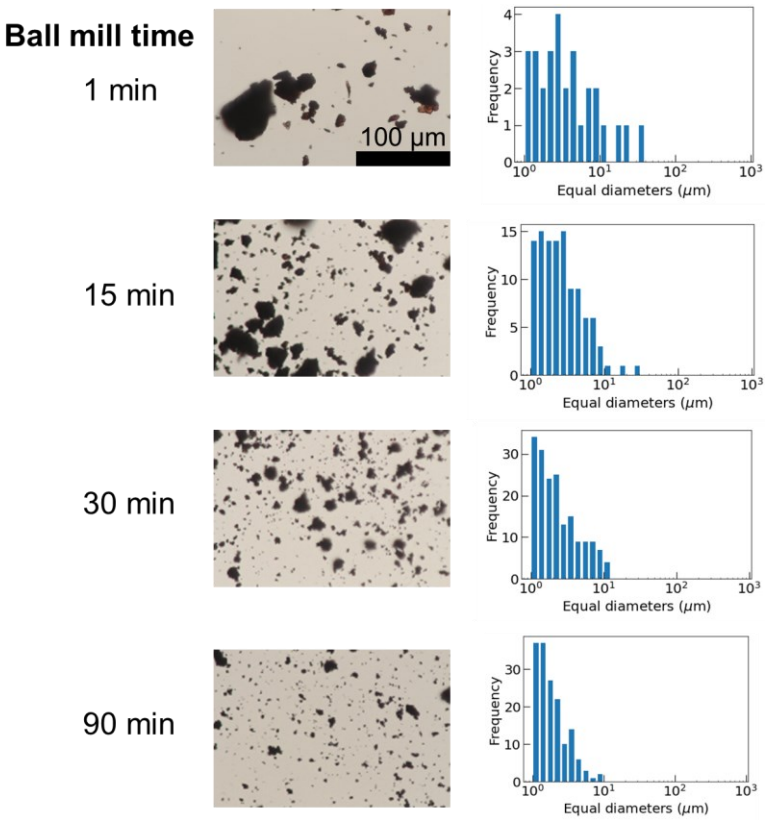


a)

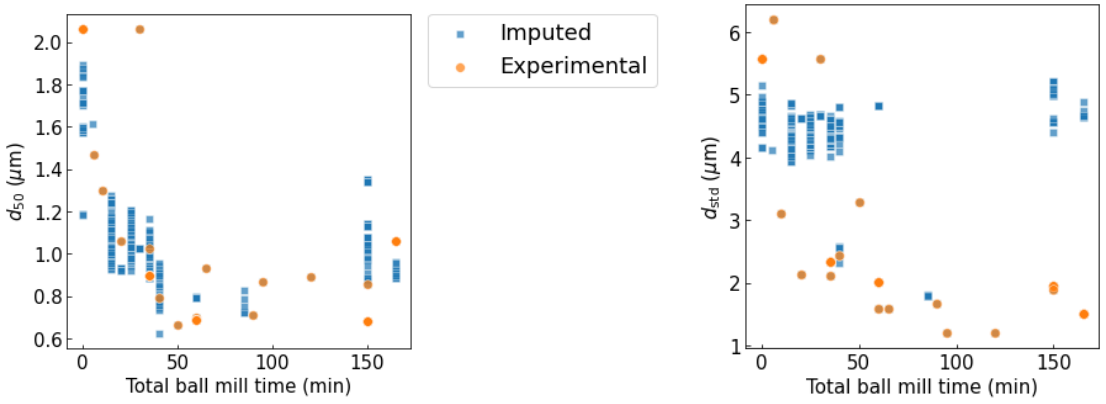


b) c)

**Supplementary Figure 7 | Particle size estimation. a,** Optical microscopy and estimated diameter distribution of sample particles. A charge-transfer complex of PMPS/chloranil = 2/1 was processed by a ball mill. **b,** Relationship between the median diameter of particles and total ball milling time during electrolyte preparation. Blue plots show values imputed by a machine learning model. **c,** Plots for the standard deviation of diameter.

**Supplementary Discussion a: Significance of essential parameters for $\sigma_{ion}$**

SHAP values for vital parameters for $\sigma_{ion}$ were calculated in Figure 3d. The scientific meanings of such variables are given below.

**F (static, MAS): FWHM** This parameter is the FWHM of a $^{19}F$ peak during static (MAS) NMR. Narrower peaks indicated higher thermal anion activity, which is essential for transporting lithium ions via thermal motion.

**F (Li) (static): $\delta$** This parameter is the chemical shift of a $^{19}F$ ($^{7}Li$) peak during static NMR. The value was determined mainly by the type of salt (i.e., LiFTFSI gave the highest performance) and slightly by interactions with charge-transfer complexes.

**Process fingerprint (sealing)** The full fingerprint name was 'temperature-machine-AMF-20N-Measure-EIS|Break-vacuum-pack-Disassemble-cell'. This parameter indicates the processes of sealing a cell with a vacuum pack, thermally annealing it in a constant temperature chamber under atmospheric conditions, breaking the seal, measuring the conductivity, and disassembling the cell. These processes increased conductivity. The most important process was thermal annealing, which improved the interface contacts. Supplementary Discussion g shows that leaving the sealed cell under air should not cause substantial water contamination.

**Li (static, MAS): FWHM** This parameter is the FWHM of a $^{7}Li$ peak during static (MAS) NMR. As discussed in the main manuscript, narrower peaks indicate higher ions mobility. The result that smaller SHAP values indicated higher conductivity was consistent with the physical model.

**Thickness** This parameter is the thickness of the electrolyte. Smaller SHAP values increased conductivity, whereas $\sigma_{ion}$ principally should not depend on the thickness. An inhomogeneous electrolyte layer that was too thick may have broken the percolation pathways.

**Melting enthalpy** This value is the melting enthalpy of salt species during DSC. Smaller SHAP values gave higher conductivity. Because the phase transition from the crystal to amorphous phases decreases the enthalpy, the trend indicates the importance of the amorphous phase for conduction.

**Formal donor ratio** This parameter is the formal molar ratio of the donor molecule in an electrolyte. Smaller SHAP values were favoured for higher conductivity because donor polymers themselves were not ionically conductive, but interacted with salt molecules.

**Date difference** This parameter is related to the time from electrolyte preparation to measurement. The parameter should be related to the long-term stability of the electrolytes. On the other hand, no obvious relation to conductivity was observed currently; further study is needed in future research.

**Temperature of $\sigma_{ion}$** This parameter is the temperature during conductivity measurements. Higher temperatures induced greater molecular motion.

***d*$_{50}$** This parameter indicates the median of electrolyte particle diameters. A smaller diameter should favour dense stacking of electrolytes, although no clear trend was detected with the SHAP values. More experimental results are needed instead of imputed results to improve the trend analysis.

**Salt weight ratio** This parameter is the weight ratio of salt molecules in an electrolyte. Larger SHAP values resulted in higher conductivity because higher salt concentration increases the number of carriers.

**Total heat time** This parameter is the total duration of heating during electrolyte preparation. Although heating is essential for conductivity, no obvious trend was observed. This indicated that optimal heating conditions (temperature, duration, and timing) were essential for performance.

**Donor MW** This parameter is the molecular weight of donor polymers. Smaller SHAP values (i.e., use of PPO) contributed to higher performances than low SHAP values (use of PMPS). The effect of

the polymer selection is discussed in the following best electrolyte section (Supplementary Discussion h).

$d_{std}$ This parameter indicates the standard deviation of electrolyte particle diameters. Smaller values favoured higher performance. Physically, smaller particles lead to denser packing and more contacts among electrolyte particles, increasing conductivity.

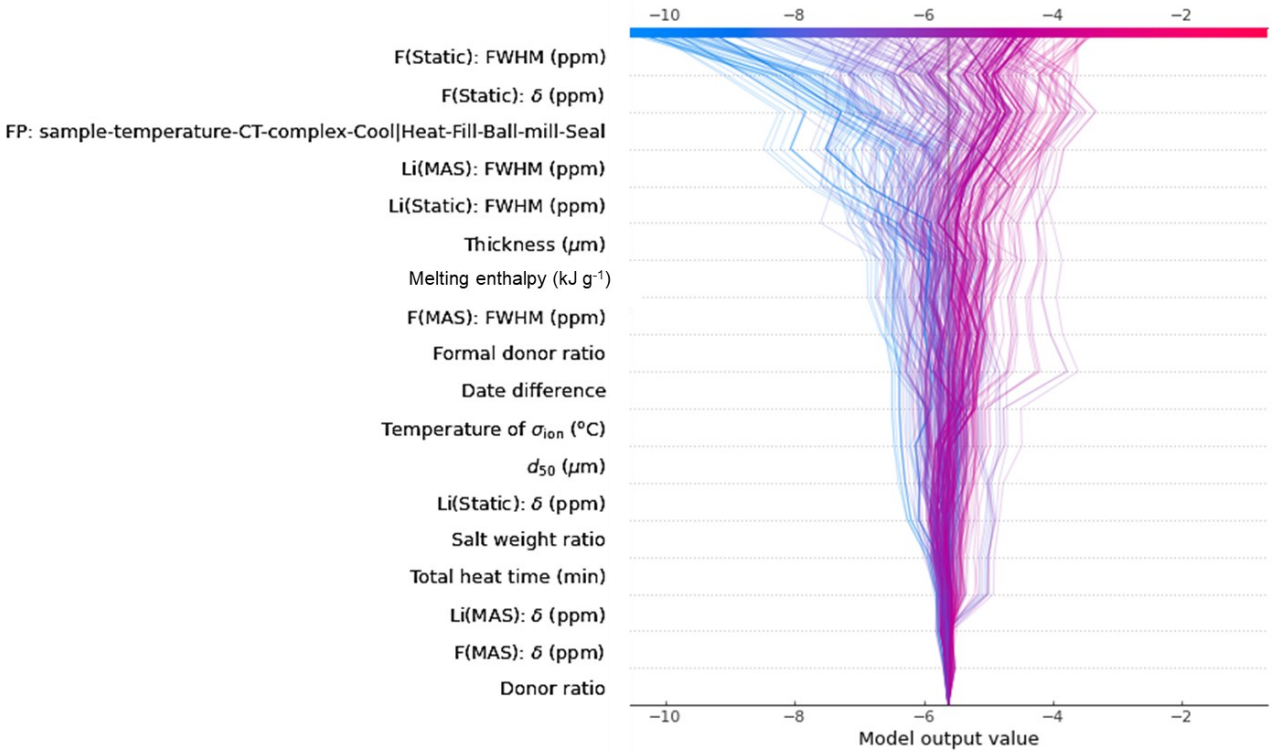


**Supplementary Figure 8 | Decision plot for the SHAP values.** A related figure is shown in Figure 3d.

**Supplementary Discussion b: Causal reasoning for electrolyte parameters**

According to the SHAP value analysis, the five primary parameters were selected manually: salt ratio, formal donor/acceptor ratio, log $\sigma_{ion}$, salt crystallinity, and FWHM of the $^{7}$Li peak (MAS NMR). Causal relationships among the experimental parameters were automatically analyzed by machine learning (Figure 3e). The analysis indicated that salt ratio and formal donor/acceptor ratio were independent variables, and the rest were dependent. The prediction was consistent with the actual experiments because the other three parameters were not directly controllable but depended on experimental conditions.

The higher salt ratio decreased the conductivity, whereas it increased crystallinity and FWHM. As discussed in the main manuscript, amorphous phases with sharp NMR peaks were attributed to ion conduction. The excess salts inhibited the phase transition from the crystal phases with lower conductivity. A higher formal donor/acceptor ratio increased the crystallinity and decreased the conductivity, indicating the important effect of acceptor molecules on the amorphous transition of salts (e.g., formation of the polarised charge-transfer complex and the interaction of polar groups in the acceptors with salts). Our results demonstrate that automated causal exploration can assist objective causal inference and improve our understanding of underlying mechanisms.

**Supplementary Discussion c: Molecular interaction analysis by DFT calculations**

Molecular-level interactions between LiFTFSI and solvating molecules were estimated by simple DFT calculations (Supplementary Figure 9). The model solvents were poly(ethylene glycol) (PEG, trimer), chloranil (two molecules), PPO (trimer), PMPS (trimer), PPO + chloranil, and PMPS + chloranil. The initial geometry for the calculation consisted of the following groups arranged near a LiTFSI lithium atom: PEG oxygen atoms, chloranil carbonyls, and the polymer aromatic rings and heteroatoms.

After structure optimization, the intramolecular distance between lithium and oxygen atoms in the anion increased from 1.8 to 1.9–2.0 Å (Supplementary Figure 10a). The longest length of 2.0 Å was observed with a common solvent, PEG, although other solvents could also work as solvents (distance of ca. 1.9 Å). Mulliken charges were also decreased by the electron-donating effects of the solvents (Supplementary Figure 10b). The original charge of 0.6 was shifted to −0.3 by PEG. The donating effect was smaller with chloranil (ca. 0.2). However, aromatic rings increased the negativity substantially (−0.5 to −0.8).

The molecular interactions were also quantified by introducing stabilization energy. The value was calculated by the energy difference between the normal state and another state where the surrounding molecules existed far from the salt (Supplementary Figure 10c). The stabilization trend almost correlated with the lithium-oxygen distance, as demonstrated by the enormous stabilization energy with PEG (180 kJ $mol^{-1}$) and moderate values with the others (60–100 kJ $mol^{-1}$). Greater stabilization and electron donation effects were observed when both donor and acceptor molecules were present. This moderately strong cation–$\pi$ and heteroatom interactions induced the phase change of the lithium salt, resulting in higher conductivity.

In the future, further calculations with different molecular geometry and precise methods are needed to understand unexplored issues, such as detailed molecular structures of clusters. An exact comparison of PPO and PMPS, which displayed similar properties in the current calculation, is also needed to clarify the conduction processes.

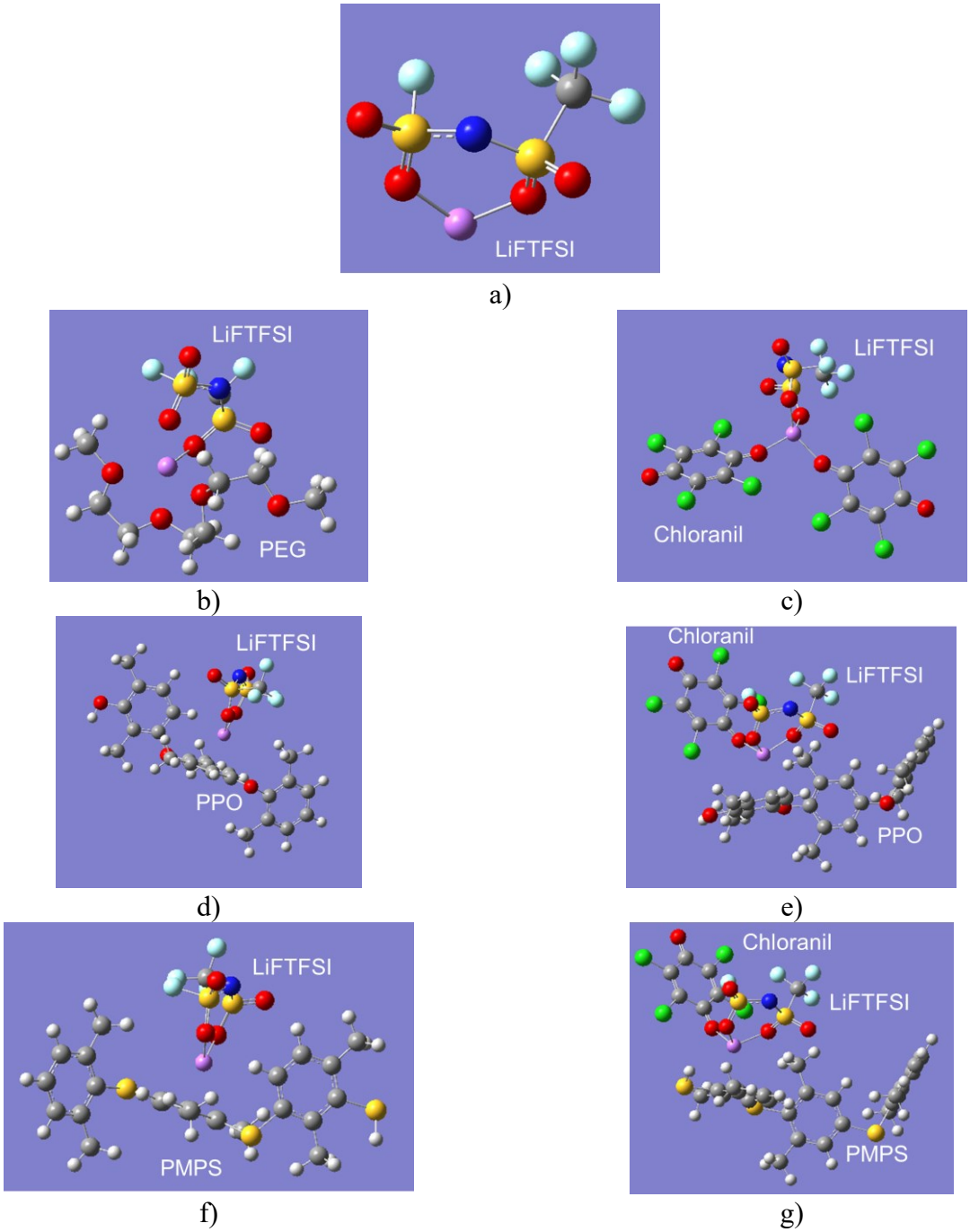


**Supplementary Figure 9 | Optimized geometry of model molecules with LiFTFSI, estimated by DFT calculations. a,** Pristine salt. **b,** PEG. **c,** Chloranil. **d,** PPO. **e,** PPO/chloranil. **f,** PMPS. **g,** PMPS/chloranil.

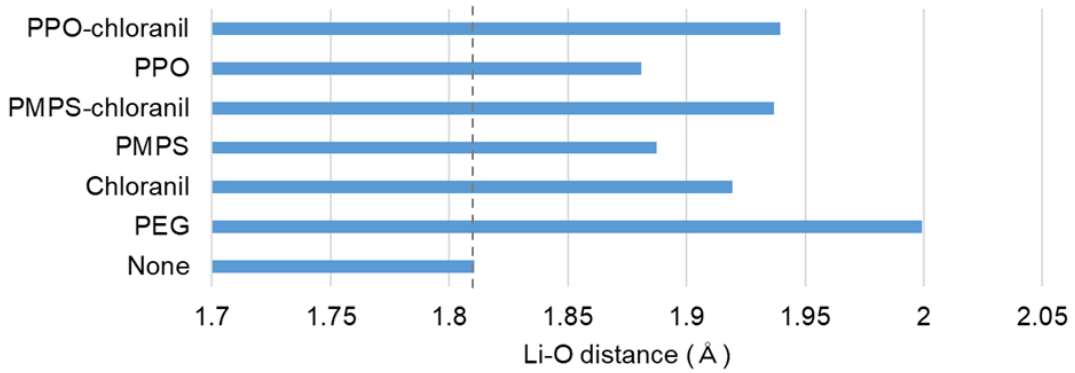


a)

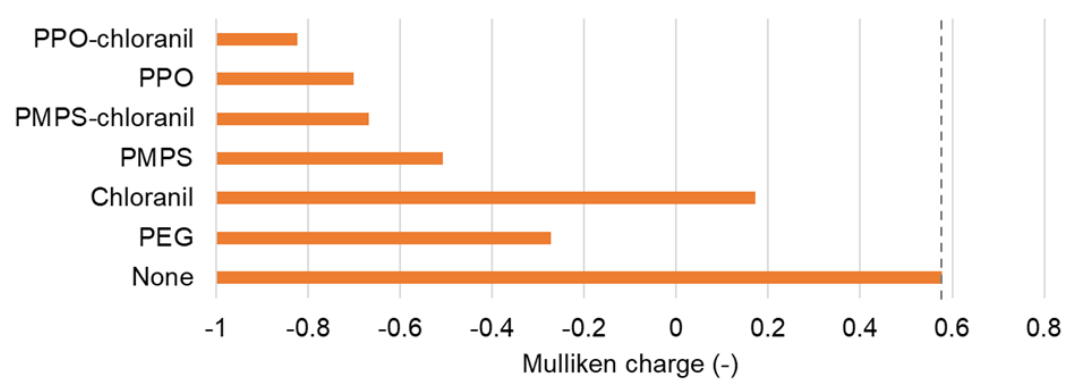


b)

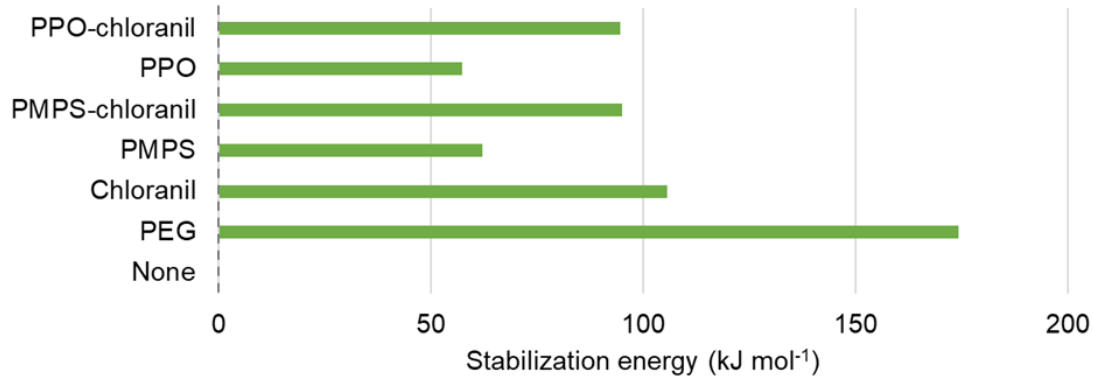


c)

**Supplementary Figure 10 | Interaction parameters estimated by DFT calculations. a,** Average distances of lithium and its neighbouring two oxygen atoms in LiFTFSI. **b,** Mulliken charge of lithium atoms. **c,** Stabilization energy. The value was defined as the energy difference between the normal structures and the control cases, where salt and surrounding molecules were far apart.

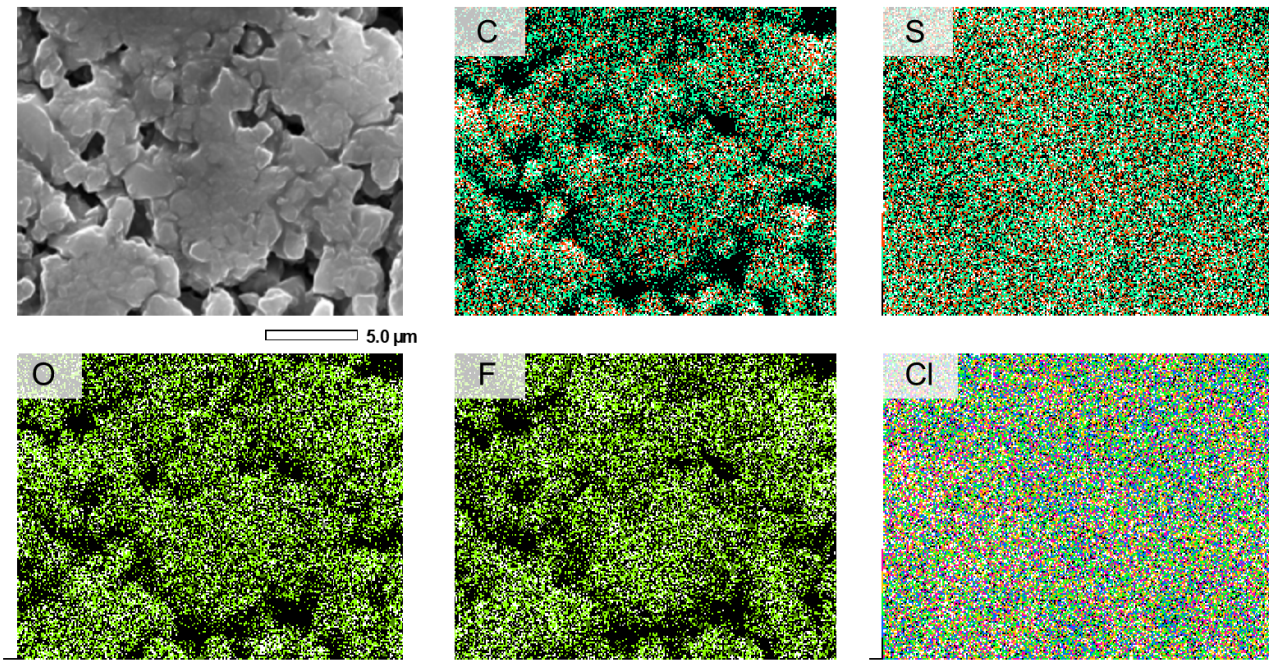


**Supplementary Figure 11 | SEM image and elemental mapping of PPO/chloranil = 6/4 (mol/mol) with 40 wt % LiFTFSI electrolyte.**

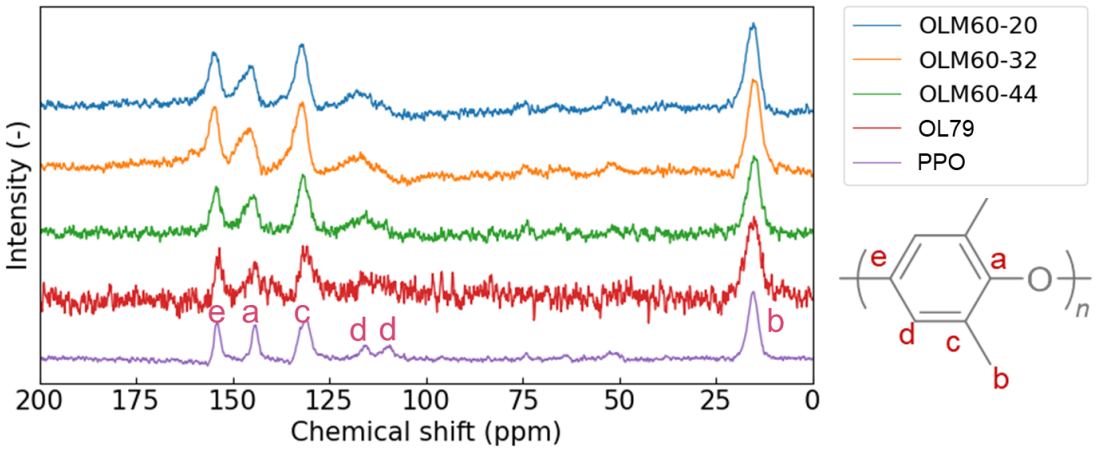
OLM60-20
OLM60-32
OLM60-44
OL79
PPO
Intensity (-)
Chemical shift (ppm)
200
175
150
125
100
75
50
25
0
e
a
c
d
d
b
e
a
O
n
d
c
b

a)

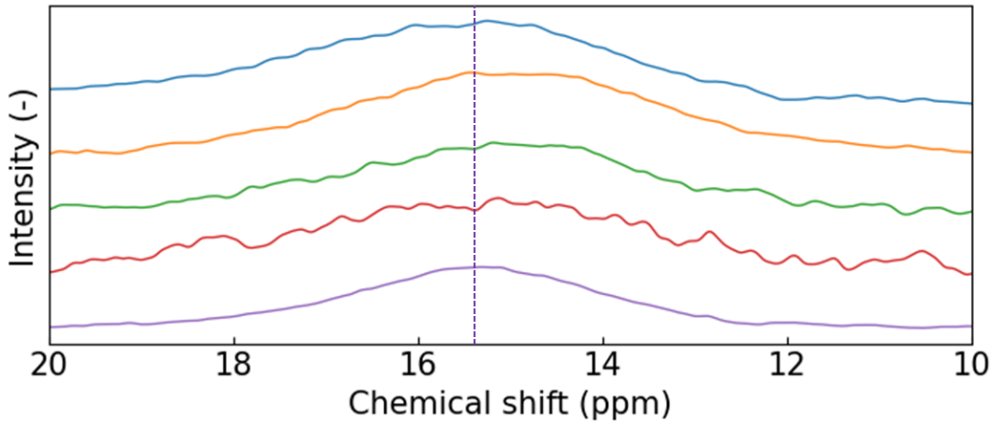
Intensity (-)
Chemical shift (ppm)
20
18
16
14
12
10

b)

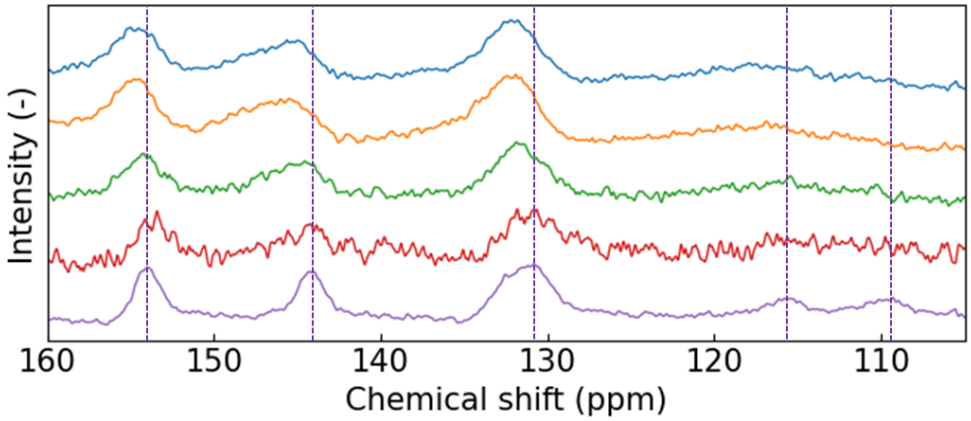
Intensity (-)
Chemical shift (ppm)
160
150
140
130
120
110

c)

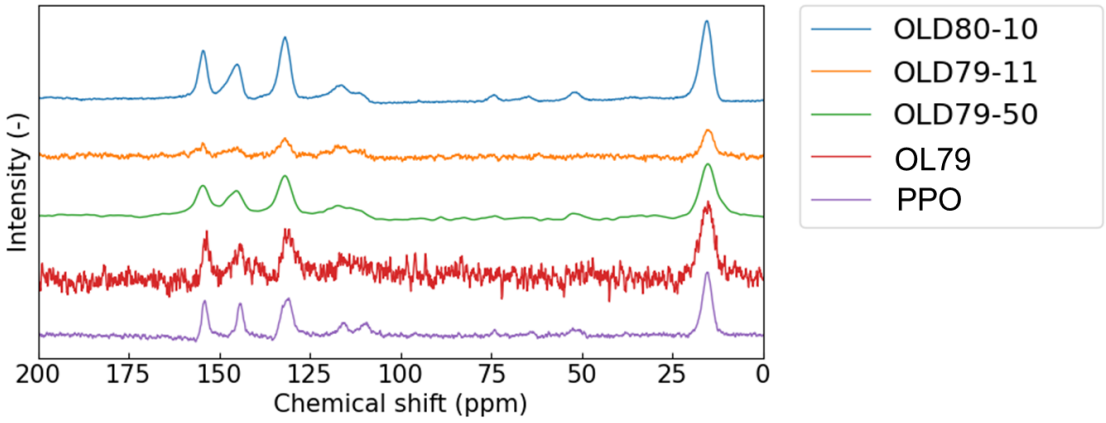


d)

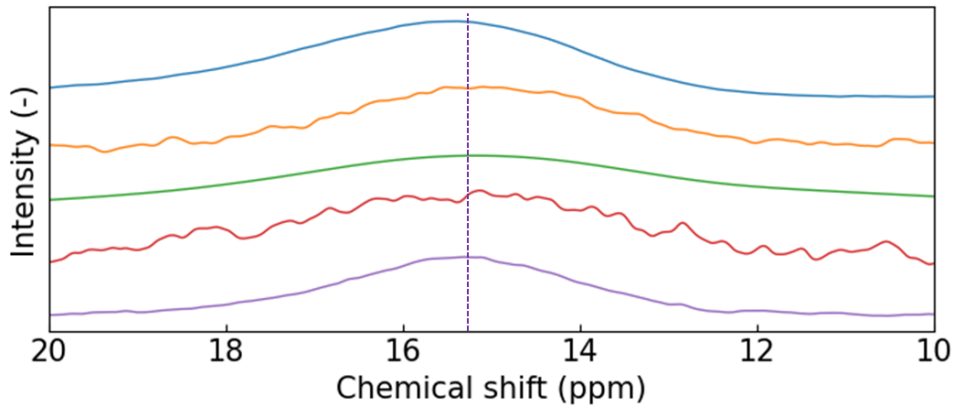


e)

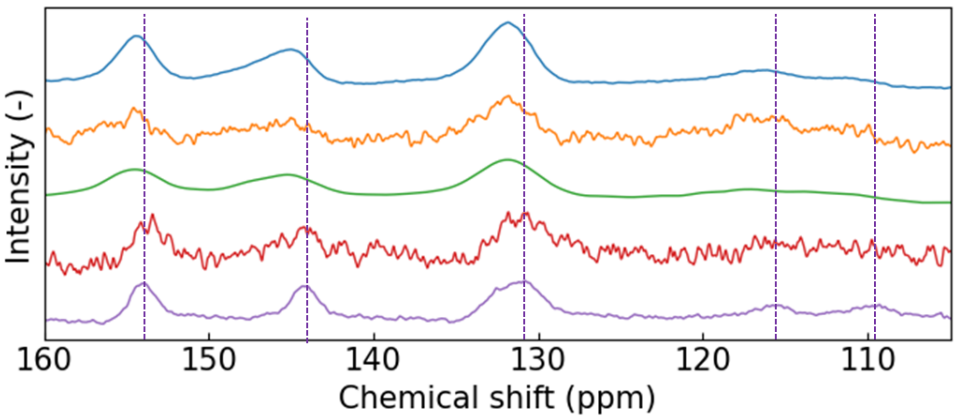


f)

**Supplementary Figure 12 | Solid-state MAS $^{13}$C-NMR spectra of samples. a,** PPO/chloranil = 60/40 (mol/mol) with LiFTFSI, charge-transfer complex (donor/acceptor = 80/20), and PPO. **b, c,** Enlargement of the spectra in **a**. **d,** Results for PPO/chloranil = 80/20 with LiTFSI. **e, f,** Enlargement of the spectra in **d**.

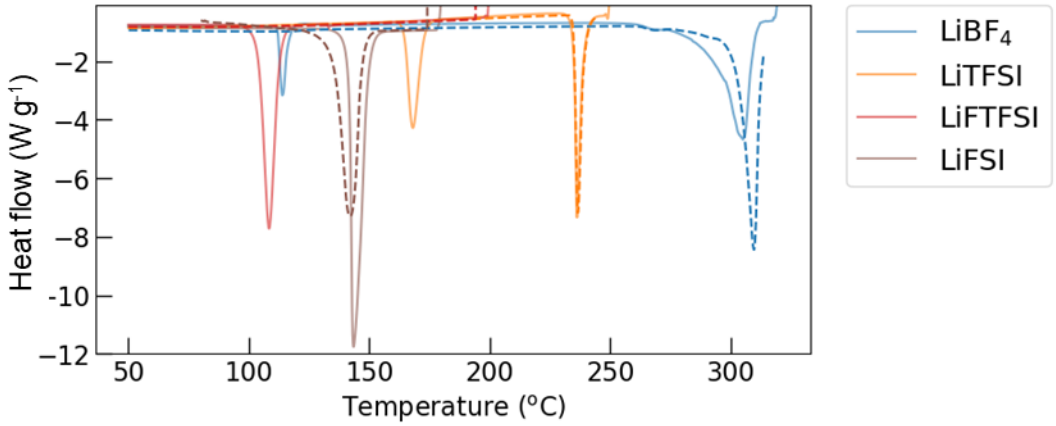
Heat flow (W g-1)
−2
−4
−6
−8
-10
−12
50
100
150
200
250
300
Temperature (°C)
LiBF4
LiTFSI
LiFTFSI
LiFSI

a)

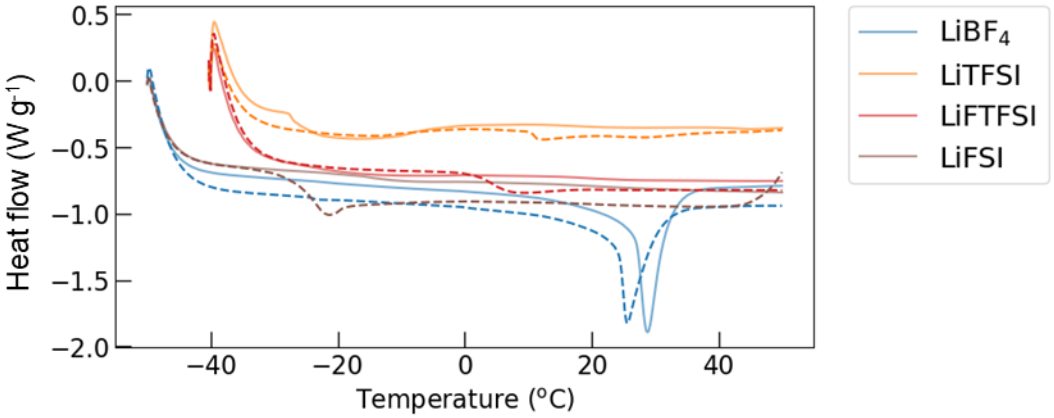
Heat flow (W g-1)
0.5
0.0
−0.5
−1.0
−1.5
−2.0
−40
−20
0
20
40
Temperature (°C)
LiBF4
LiTFSI
LiFTFSI
LiFSI

b)

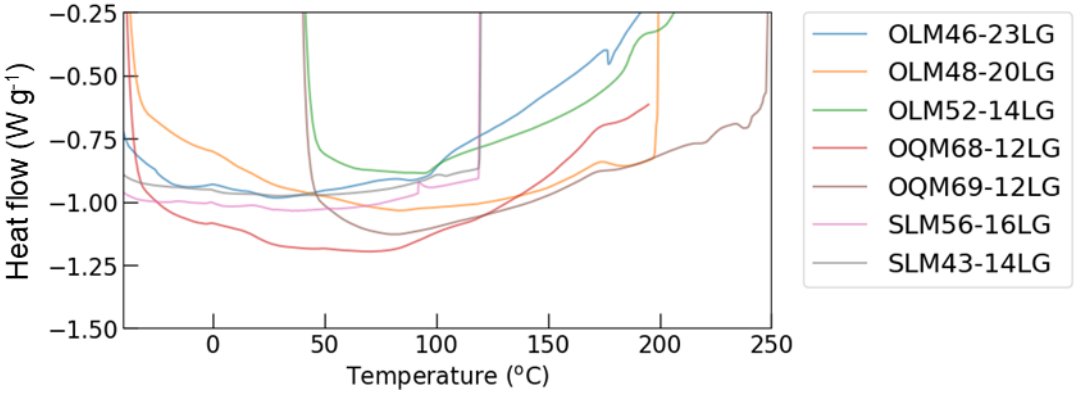
Heat flow (W g-1)
−0.25
−0.50
−0.75
−1.00
−1.25
−1.50
0
50
100
150
200
250
Temperature (°C)
OLM46-23LG
OLM48-20LG
OLM52-14LG
OQM68-12LG
OQM69-12LG
SLM56-16LG
SLM43-14LG

c)

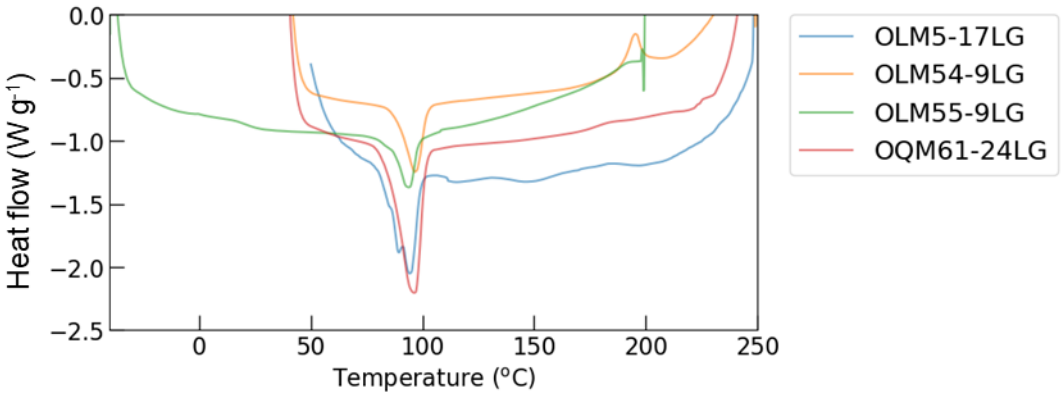


d)

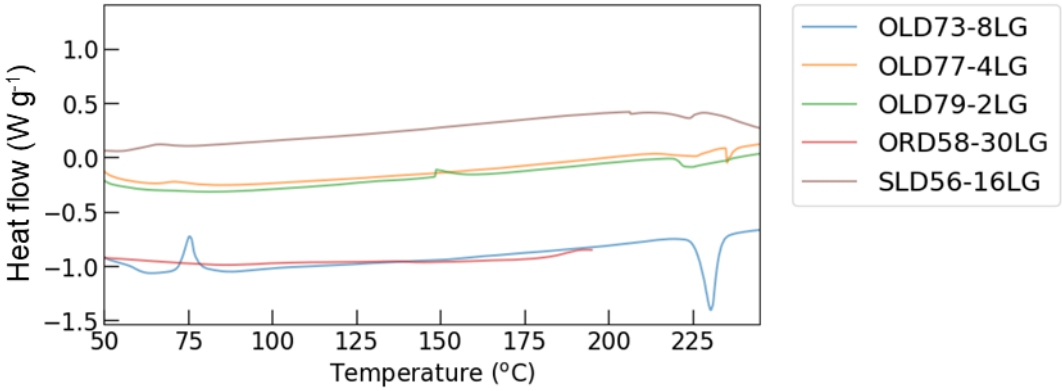


e)

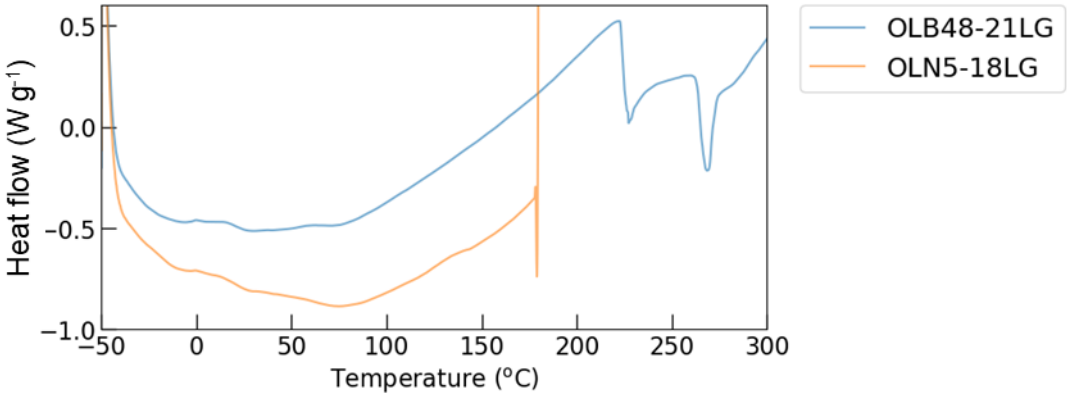


f)

**Supplementary Figure 13 | DSC curves of samples. a,** Pristine salts. Solid and dashed lines represent the first and second cycles, respectively. **b,** Results for the low-temperature region. LiFTFSI electrolytes **c,** with small melting peaks and **d,** with detectable peaks. **e,** LiTFSI electrolytes. **f,** $LiBF_4$ and LiFSI electrolytes. The scan rate was 20°C $min^{-1}$. Detection of $T_g$ peaks of salts was difficult with electrolytes because of the fluctuating baselines for the polymers.

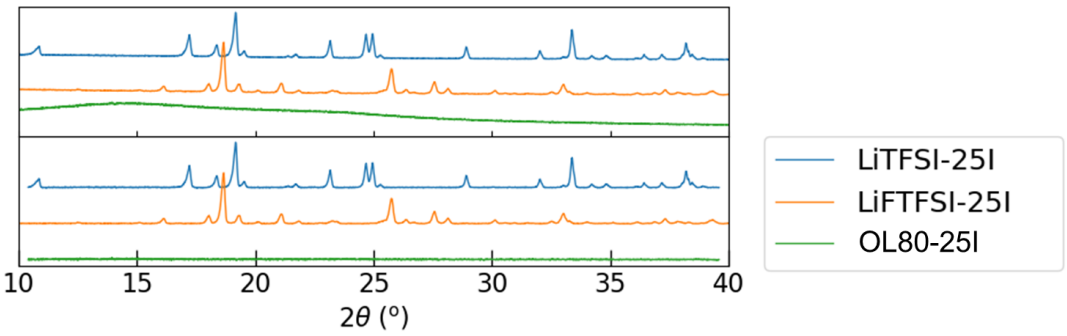


a)

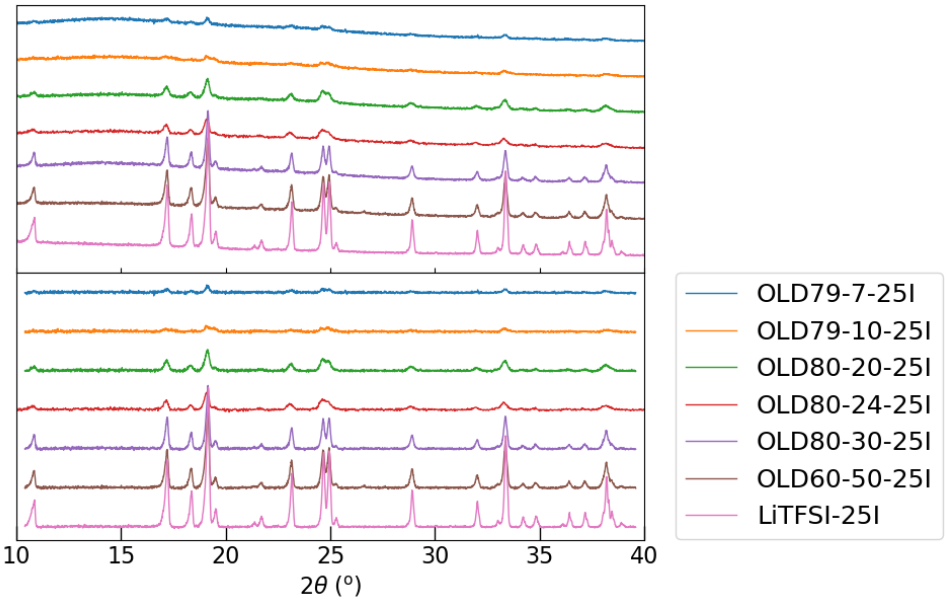


b)

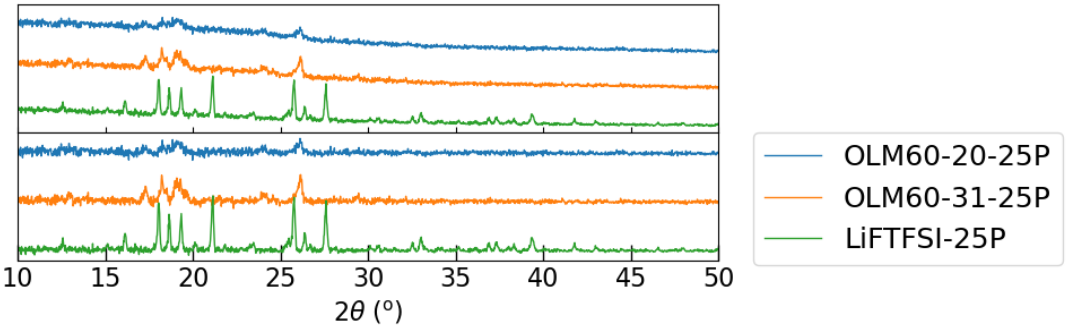


c)

**Supplementary Figure 14 | XRD spectra of samples measured at room temperature.** The samples were named using the format 'XXX-NNY', where XXX was the electrolyte measured at NN°C by method Y (I: intense beam; P: parallel beam). **a,** Pristine salts and charge-transfer complex. **b,** LiTFSI

electrolytes. **c,** LiFTFSI electrolytes. Original peak data are shown in the upper graphs, and backgrounds are removed in the bottoms.

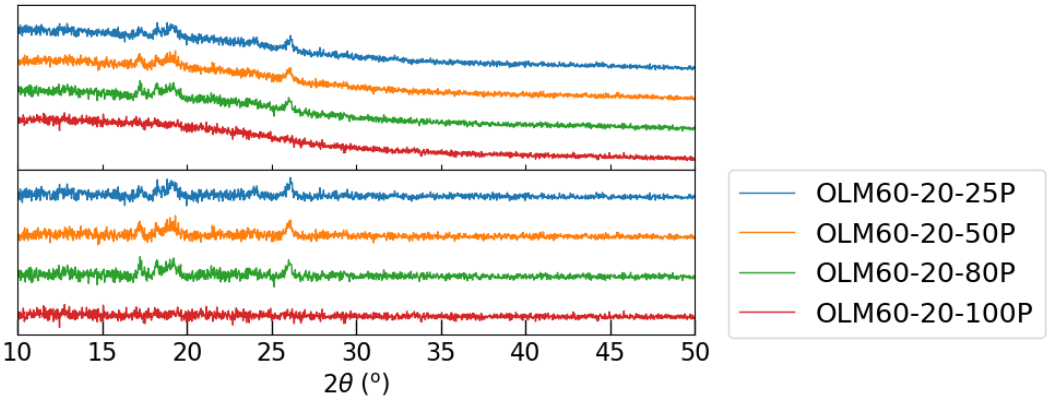
OLM60-20-25P
OLM60-20-50P
OLM60-20-80P
OLM60-20-100P
10 15 20 25 30 35 40 45 50
2θ (°)

a)

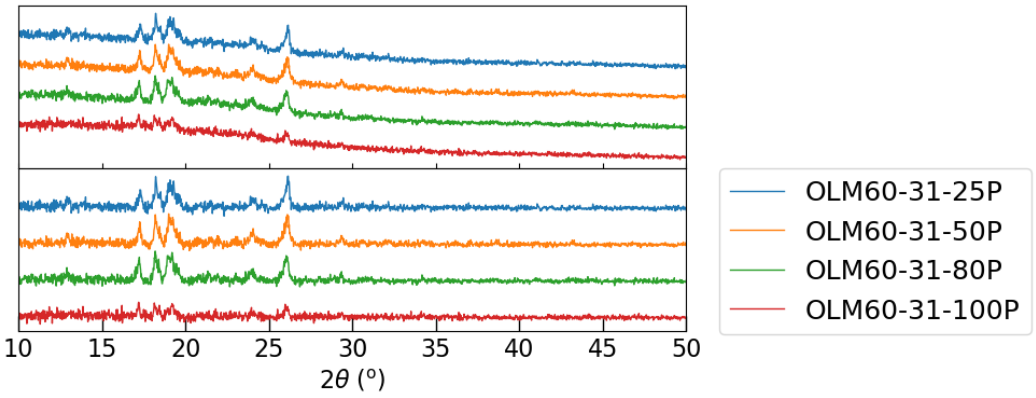
OLM60-31-25P
OLM60-31-50P
OLM60-31-80P
OLM60-31-100P
10 15 20 25 30 35 40 45 50
2θ (°)

b)

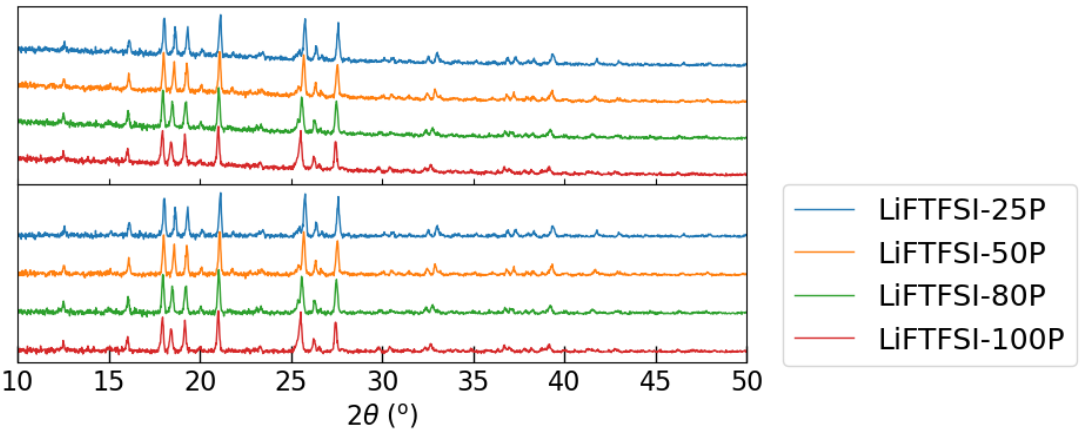
LiFTFSI-25P
LiFTFSI-50P
LiFTFSI-80P
LiFTFSI-100P
10 15 20 25 30 35 40 45 50
2θ (°)

c)

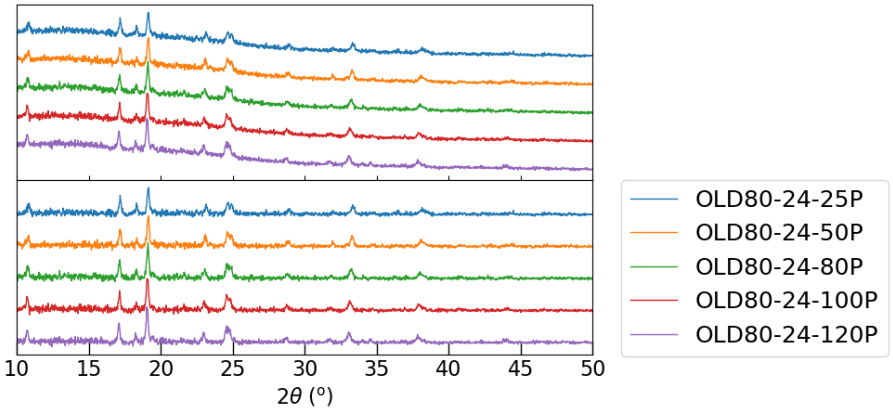


d)

**Supplementary Figure 15 | Temperature dependence of XRD spectra. a,** PPO/chloranil = 60/40 with 20 wt % LiFTFSI. **b,** PPO/chloranil = 60/40 with 31 wt % LiFTFSI. **c,** Pristine LiFTFSI. **d,** PPO/chloranil = 80/20 with 24 wt % LiTFSI. Original peak data are shown in the upper graphs, and backgrounds are removed in the bottoms.

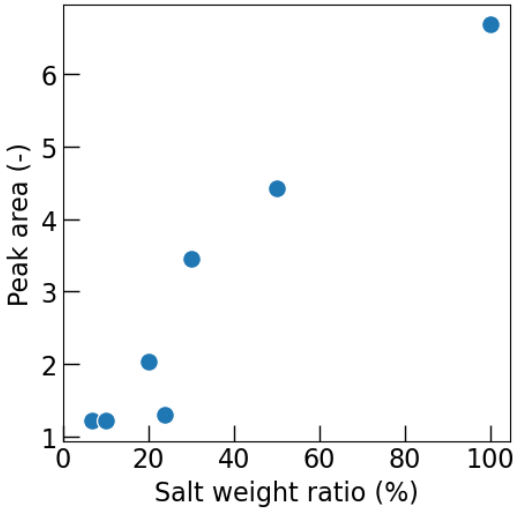


**Supplementary Figure 16 | Relationship between salt weight ratio and signal peak areas in XRD spectra.** The signals of PPO/chloranil/LiTFSI electrolytes in Supplementary Figure 14b were analyzed.

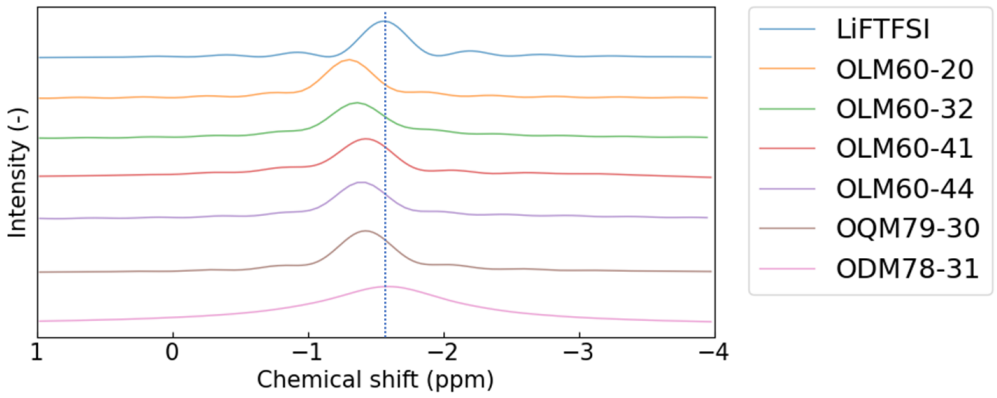


a)

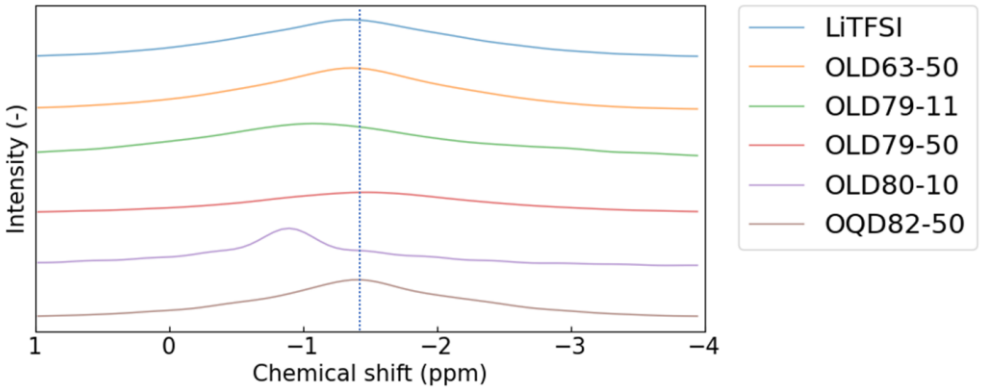


b)

**Supplementary Figure 17 | Solid-state $^{7}$Li MAS NMR spectra of samples. a,** LiFTFSI electrolytes. **b,** LiTFSI electrolytes.

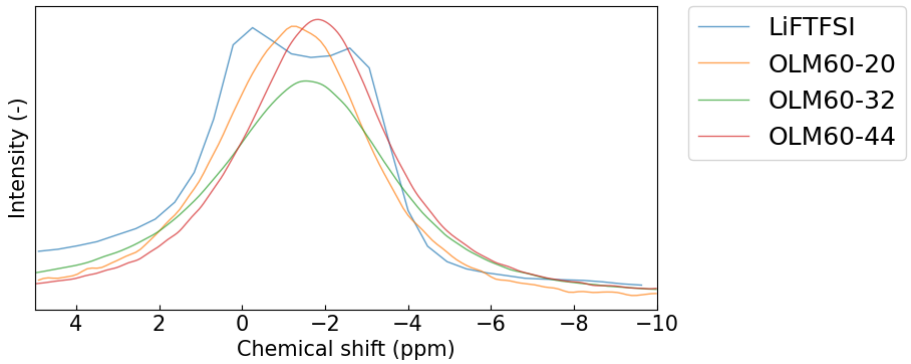


**Supplementary Figure 18 | Solid-state $^{7}$Li NMR spectra of samples.** NMR tubes did not rotate during the measurements (static measurements).

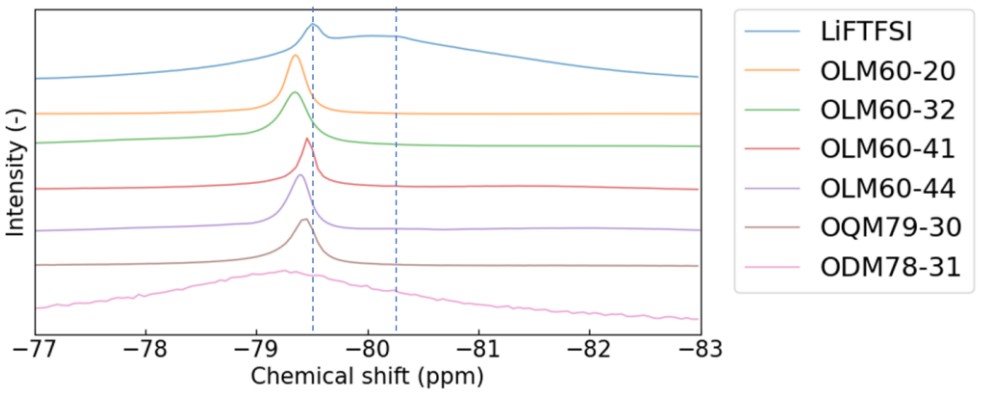


a)

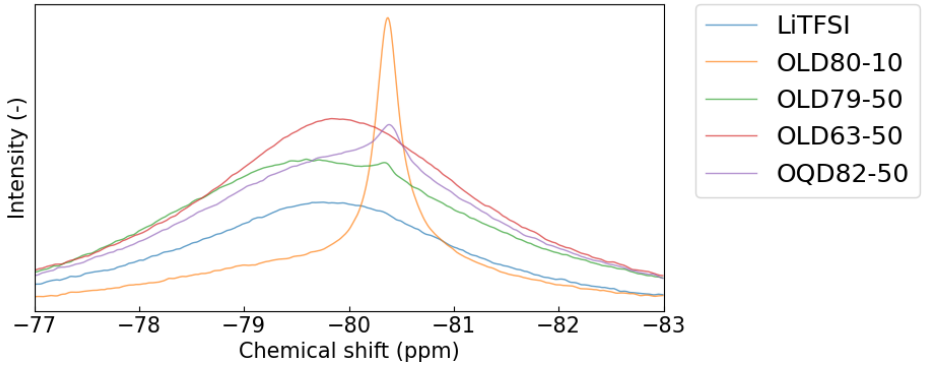


b)

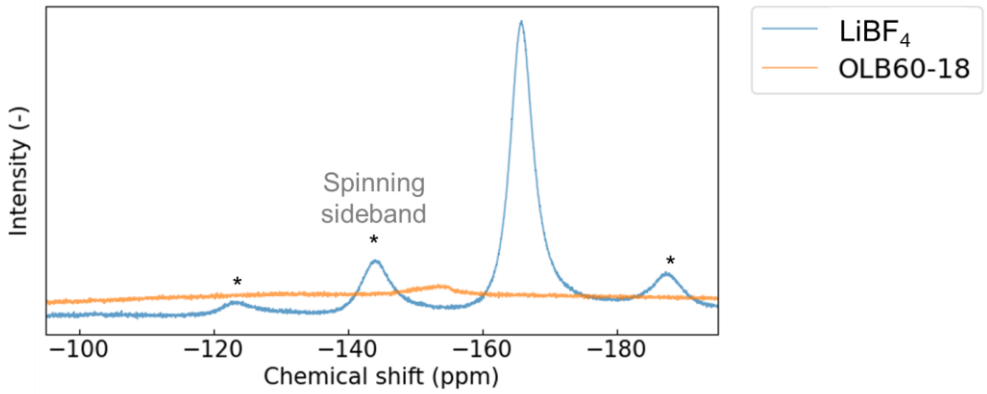


c)

**Supplementary Figure 19 | Solid-state $^{19}$F MAS NMR spectra of samples. a,** LiFTFSI electrolytes. **b,** LiTFSI electrolytes. **c,** $LiBF_4$ and its electrolyte (no peaks were detected for the electrolyte).

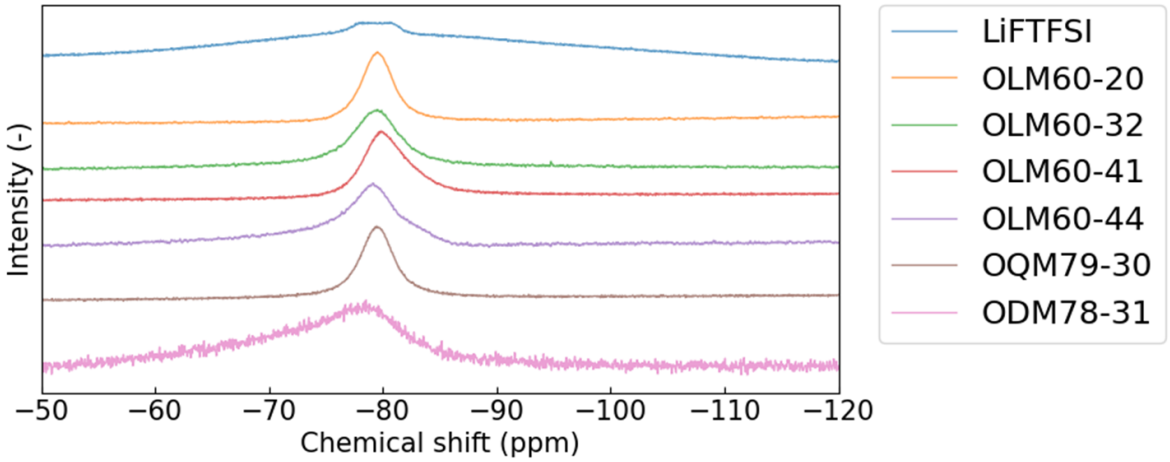


**Supplementary Figure 20 | Solid-state $^{19}$F NMR spectra of LiFTFSI samples.** NMR tubes did not rotate during the measurements (static measurements).

**Supplementary Discussion d: Relaxation time estimation by solid-state NMR**

The relaxation processes of atoms in some electrolytes (OLM60-31, OLM60-40, OQM79-30) and LiFTFSI were investigated by solid-state static NMR. $^{7}$Li peaks of the electrolytes became sharper after increasing the measurement temperatures (25 to 80°C, Supplementary Figure 21a). Similarly, sharp components in the $^{19}$F peaks became more significant at elevated temperatures (Supplementary Figure 21b). Thermal activated atomic motions induced the longer spin-spin relaxation time, resulting in the peak sharpening.

FWHM of $^{7}$Li peaks was analyzed as a temperature function (Supplementary Figure 21c). The value was around 3 kHz at room temperature regardless of the samples. The FWHM of the electrolytes decreased to less than 1 kHz by heating. The values converged to about 0.8 kHz at 60−80°C, comparable to the conductivity trend (Supplementary Figure 22). In contrast, the FWHM of LiFTFSI was almost constant even at high temperatures, indicating that lithium cations in the salt were trapped firmly.

$T_1$ relaxation time was estimated by a saturation recovery method. In the case of $^{7}$Li, $T_1$ of the three electrolytes (0.1−1 s) was much smaller than LiFTFSI (ca. 100 s, Supplementary Figure 21d). The decrease of $T_1$ along with the heating and the smaller values than LiFTFSI meant that faster lithium atom motions were achieved in the electrolytes than in pristine salt.

Even with $^{19}$F atoms, a shorter relaxation time was observed with the electrolytes (ca. 1 s) than the pure salt (ca. 10 s, Supplementary Figure 21e). The $T_1$ time of the electrolytes was almost constant at 25−80°C, while the pristine LiFTFSI crystal exhibited a decreasing trend; the pure salt needed additional thermal energy for more active motions (i.e., for smaller $T_1$). The small $T_1$ of the electrolytes suggested that thermal motions of fluorine groups (e.g., rotation of $CF_3$) were significant even at room temperature. The molecular motions of fluorine atoms in anionic species, probably associated with charge-transfer complexes, could be a key to ionic conductivity observed in this study.

Pulsed-field gradient NMR for estimating the diffusion coefficients of atoms was not possible the fast spin-spin relaxation. The electron spins in the charge-transfer complexes or trace amounts of metals contaminated during ball milling may have interfered with the measurement, which should be clarified in future work.

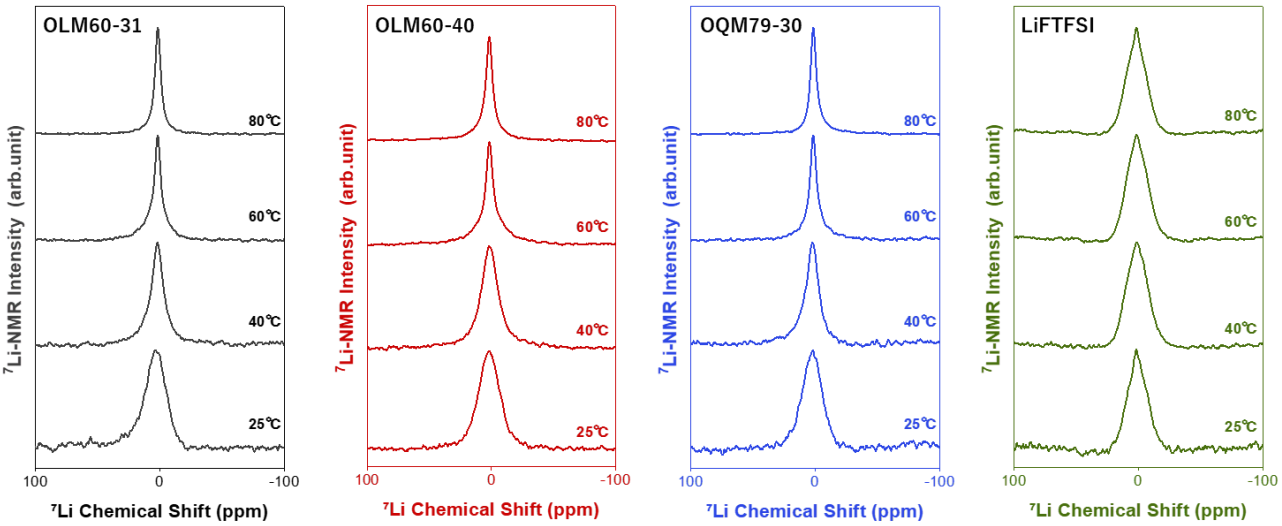
OLM60-31
OLM60-40
OQM79-30
LiFTFSI
80℃
60℃
40℃
25℃
7Li-NMR Intensity (arb.unit)
100
0
-100
7Li Chemical Shift (ppm)

a)

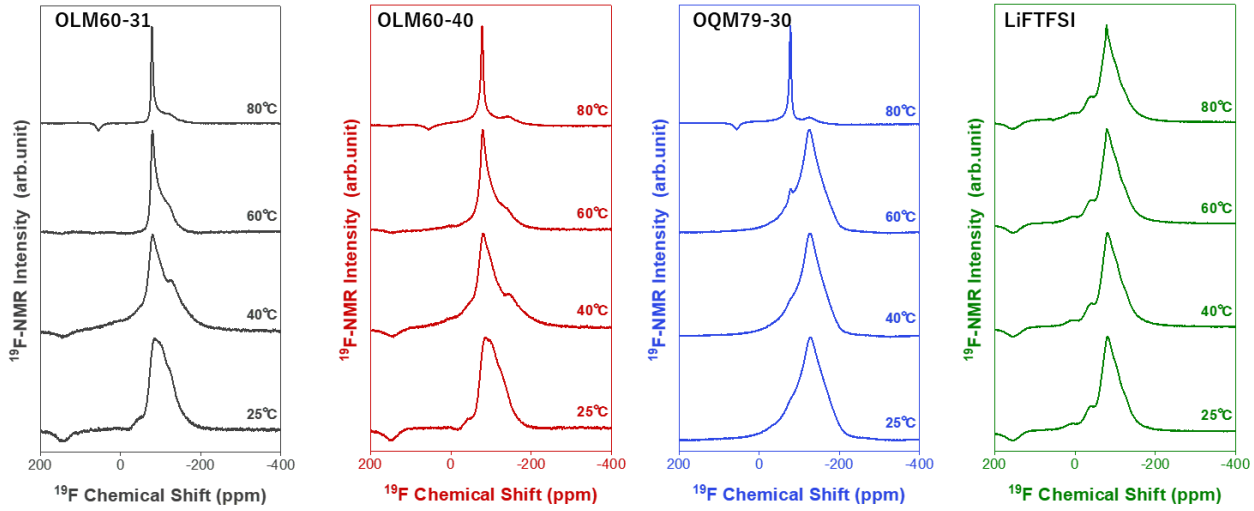
OLM60-31
OLM60-40
OQM79-30
LiFTFSI
80℃
60℃
40℃
25℃
19F-NMR Intensity (arb.unit)
200
0
-200
-400
19F Chemical Shift (ppm)

b)

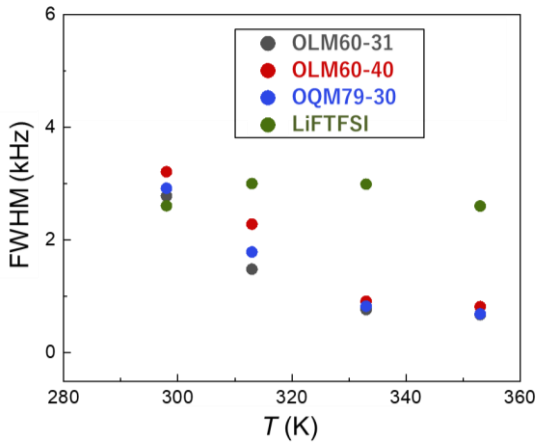


c)

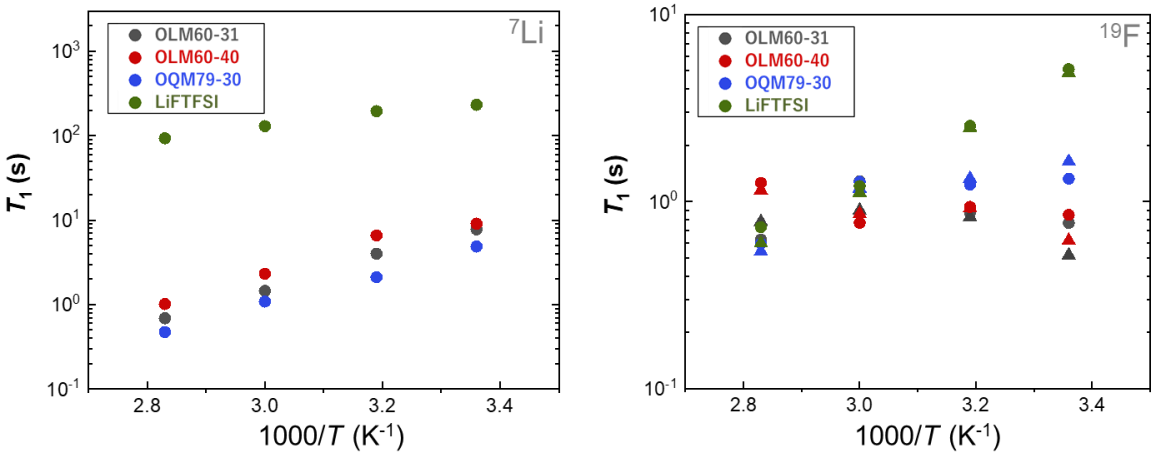


d) e)

**Supplementary Figure 21 | Relaxation time estimation of by solid-state NMR.** a, $^{7}$Li NMR spectra for OLM60-31, OLM60-40, OQM79-30 and LiFTFSI with different temperatures. b, $^{19}$F NMR Spectra. c, FWHM of $^{7}$Li peaks. d, Arrhenius plots of $T_1$ relaxation time for $^{7}$Li. e, Arrhenius plots for $^{19}$F. Circle and triangle plots correspond to the broad (ca. -120 ppm) and sharp (ca. -80 ppm) $CF_3$ peaks, respectively.

**Supplementary Discussion e: Temperature dependence of ionic conductivity**

Temperature dependencies of $\sigma_{ion}$ were examined with several electrolytes (Supplementary Figure 22). In most cases, convex upward curves were observed with Arrhenius plots, indicating that the structure changes with heating or amorphous phase conduction. Successful fitting was achieved with OQM80-50, OLM60-40, and OLM60-20 (blue fitting lines), whereas the errors were not negligible for the other conditions (red lines). Some LiTFSI and LiFTFSI electrolytes suffered from unexpected conductivity decrease at higher temperatures, which could not be explained by standard Arrhenius or VFT models. The decrease was attributed to microscopic structure change in the inhomogeneous electrolytes at higher temperatures ($1000T^{-1} \cong 3\ K^{-1}$, corresponding to 60°C). The temperature was higher than the estimated $T_g$ of LiTFSI and LiFTFSI (0−10°C, Supplementary Figure 13b), where molecular motion occurred actively. No major changes in the diffraction peaks were detected by XRD (Supplementary Figure 14), but structure analyses will elucidate the mechanism in future work.

In contrast to the sulfonyl imide electrolytes, an almost linear fitting line was obtained with a $LiBF_4$ electrolyte (OLB60-18), which contained a salt that did not display a clear glass transition (Supplementary Figure 13). The amorphous phase, which is key for ionic conduction, was difficult for the symmetrical and compact $BF_4$ anion to form.

The estimated VFT parameters, apparent activation energy $B$, Kauzmann temperature $T_K$, and prefactor $\sigma_0$, were comparable for the successful fitting cases (Supplementary Figure 22c and d). For instance, $T_K$, ranged from −70°C to −50°C, corresponding to the experimental $T_g$ of 0°C–10°C with a general law of $T_g \cong T_K + 50$. The agreement indicated that the thermal motion of salt molecules themselves was essential to conduction and that the polymer and acceptor molecules induced the structure changes and other side effects.

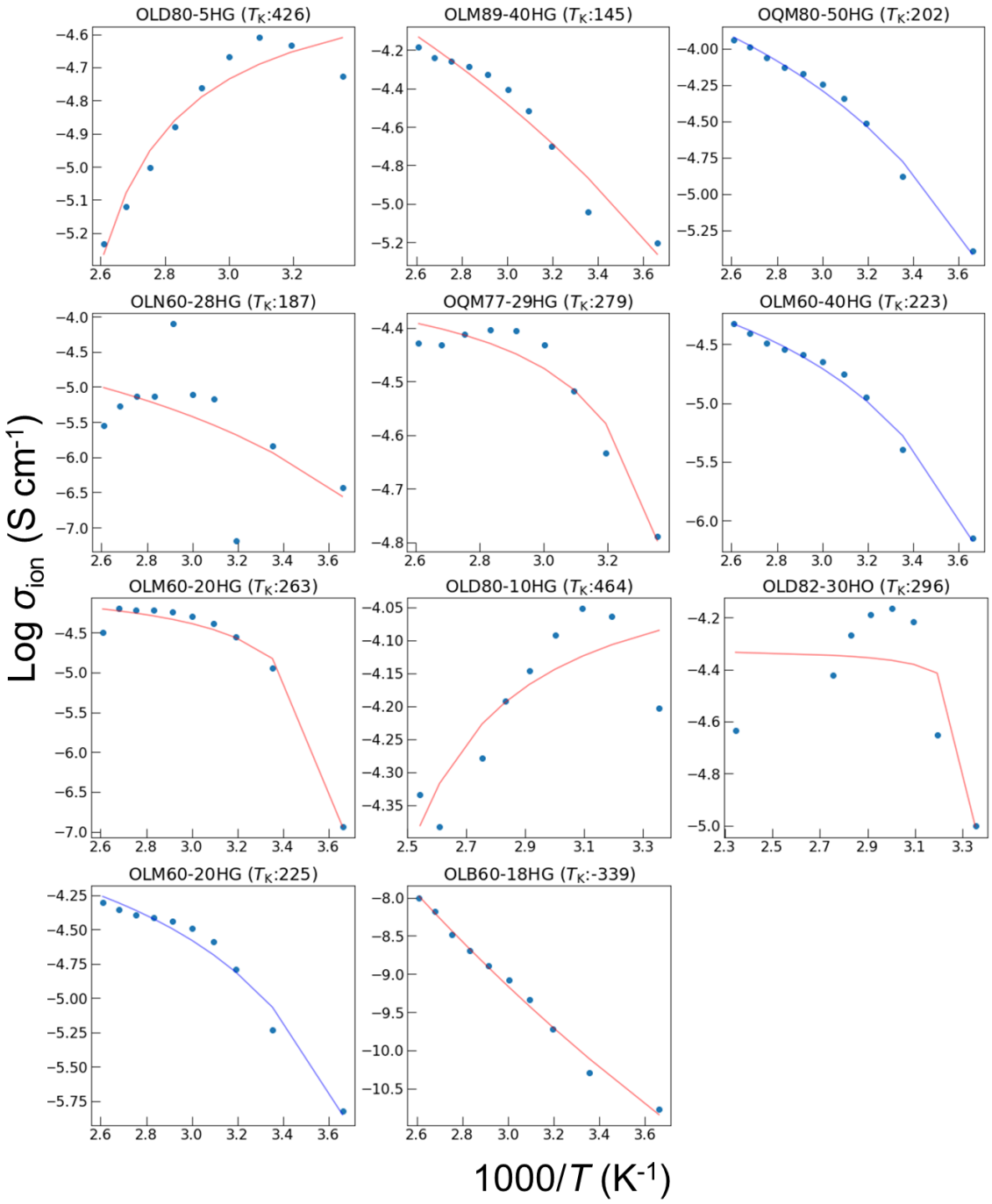
OLD80-5HG ($T_K$:426)
OLM89-40HG ($T_K$:145)
OQM80-50HG ($T_K$:202)
OLN60-28HG ($T_K$:187)
OQM77-29HG ($T_K$:279)
OLM60-40HG ($T_K$:223)
OLM60-20HG ($T_K$:263)
OLD80-10HG ($T_K$:464)
OLD82-30HO ($T_K$:296)
OLM60-20HG ($T_K$:225)
OLB60-18HG ($T_K$:-339)
Log $\sigma_{ion}$ (S cm$^{-1}$)
1000/$T$ (K$^{-1}$)

a)

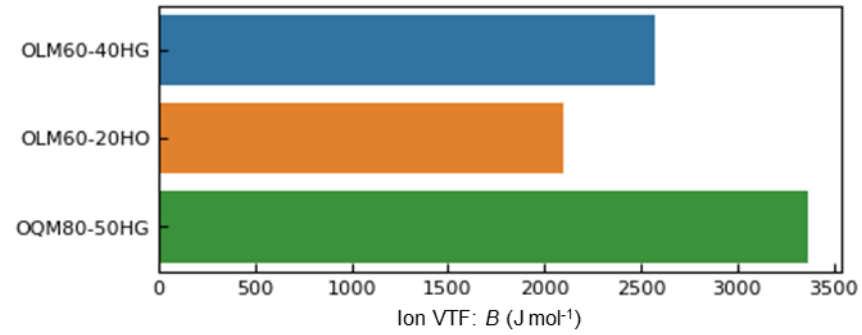


b)

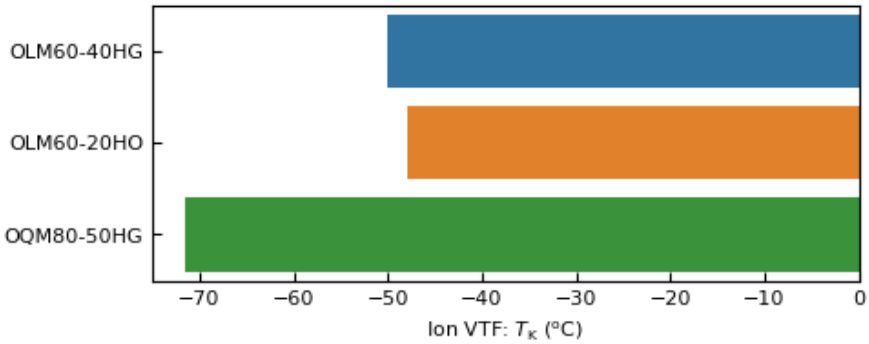


c)

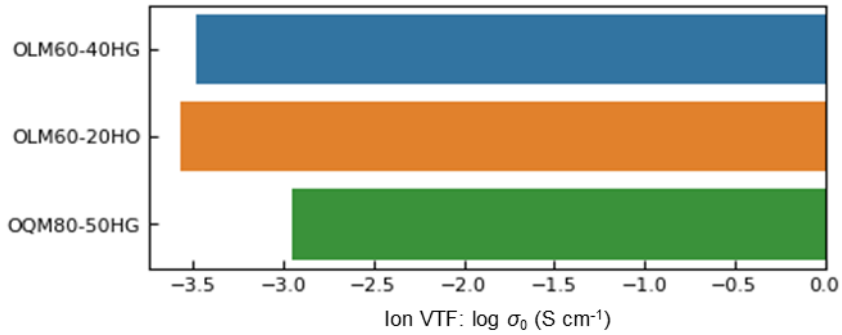


d)

**Supplementary Figure 22 | Temperature dependence analysis of electrolytes. a,** Conductivity versus temperature. Blue plots and solid lines show experimental and VFT fitting results. Fittings with significant errors are shown in red. **b,** Estimated apparent activation energy ($B$) with successful fittings. **c,** Kauzmann temperature ($T_K$). **d,** Prefactor ($\sigma_0$).

**Supplementary Discussion f: Molecular dynamics simulation of LiTFSI**

Molecular dynamics simulations were conducted for the crystal and amorphous phases of LiTFSI (Supplementary Figure 23). The salt was selected instead of LiFTFSI because public crystallographic data was available for LiTFSI. The amorphous phase was generated by locating the salt molecules randomly. Conventional calculation settings with a Lennard-Jones potential and Dreiding force field were used, which should be sufficient for the semi-quantitative comparison of the different phases. The absolute values of the movement distance or mean square displacement (MSD) of atoms were less important because the interaction parameters were not optimized.

In the crystal phase, the Li, F, and O atoms did not change substantially from their original conformation, even after 200 ns, indicating strong ion trapping (Supplementary Figure 23a). In contrast, the locations of lithium cations and anion molecules changed from their original positions by their thermal motions. The cations could hop to space by rotational and vibrational movements of anionic species.

Although calculations were semi-quantitative (i.e., potentials were not optimized), MSD can be a criterion for atom mobility (Supplementary Figure 23b). MSD of atoms in the crystal phase was almost zero ($<< 1$ Å$^2$) because the ions were trapped. On the other hand, MSD increased almost linearly with the calculation time and reached around 3 Å$^2$ (Li and O atoms) and 8 Å$^2$ (F atoms) after the calculation. MSD of F was higher than those of Li and O because of the smaller electrostatic interaction and greater flexibility of the bonds. Although the actual systems incorporated the interactions with charge-transfer complexes, the amorphous phase seems a key to transporting ions in the salt molecules.

Free volumes can also explain the different mobilities in the phases. The density of the amorphous phase (around 1.97 g cm$^{-3}$) was much smaller than that of the crystal phase (around 2.18 g cm$^{-3}$). Voids were formed in the amorphous phase, playing essential roles in transporting cations.

Higher-accuracy calculations, including the effects of donor and acceptor molecules with more realistic interaction potentials, will provide detailed insights into the conduction processes in future research.

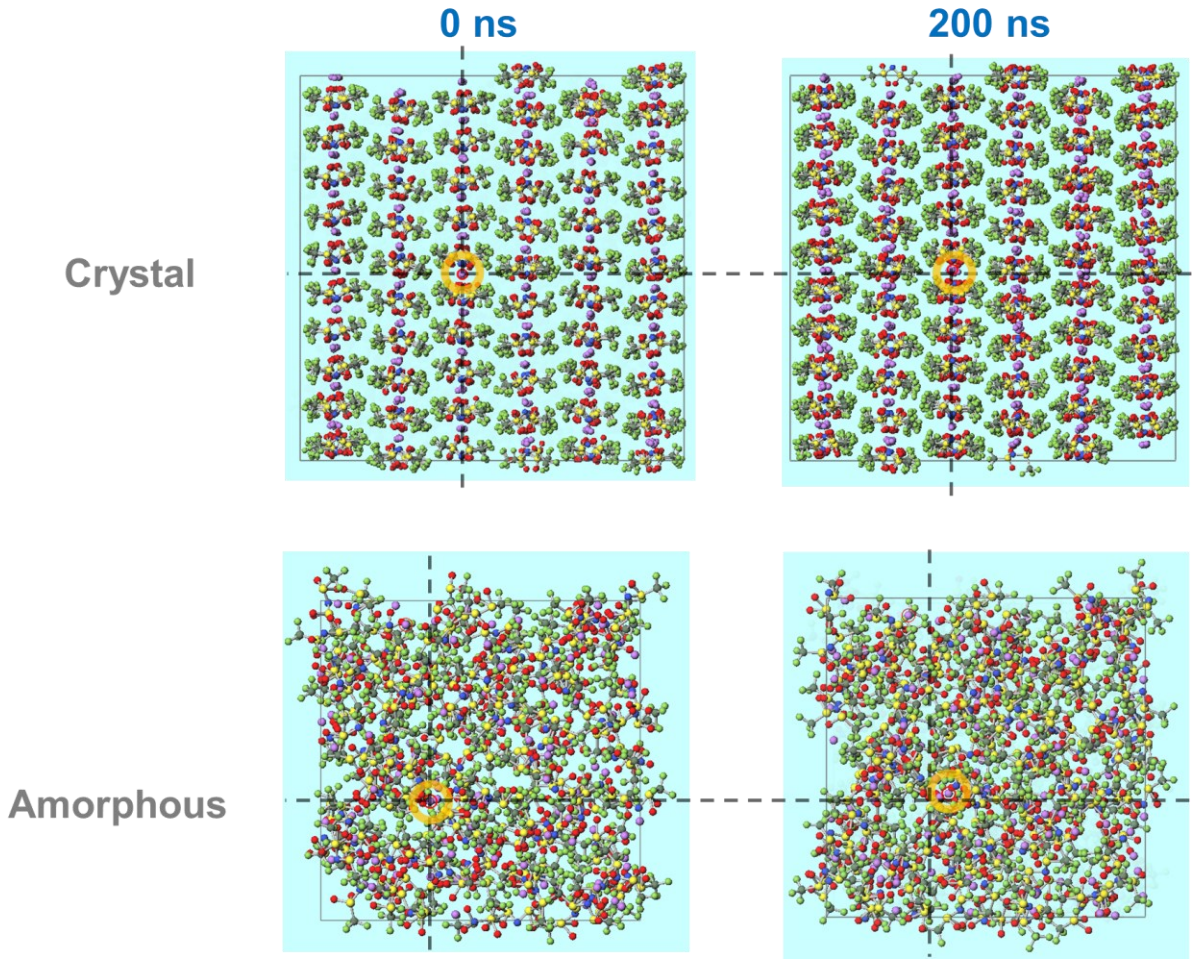


a)

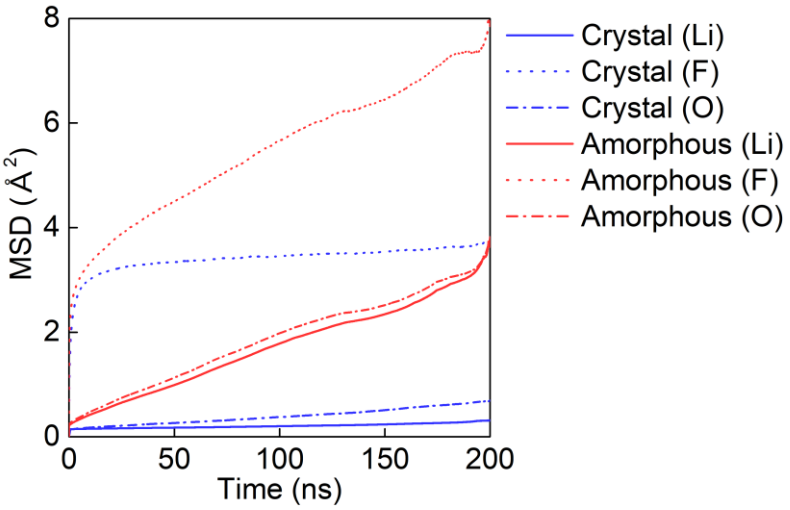


c)

**Supplementary Figure 23 | Molecular dynamics simulation of crystalline and amorphous LiFTFSI. a,** Molecular structures before/after calculation. Positions of representative lithium atoms are shown in the figures. **b,** MSD of lithium and fluorine atoms in different phases.

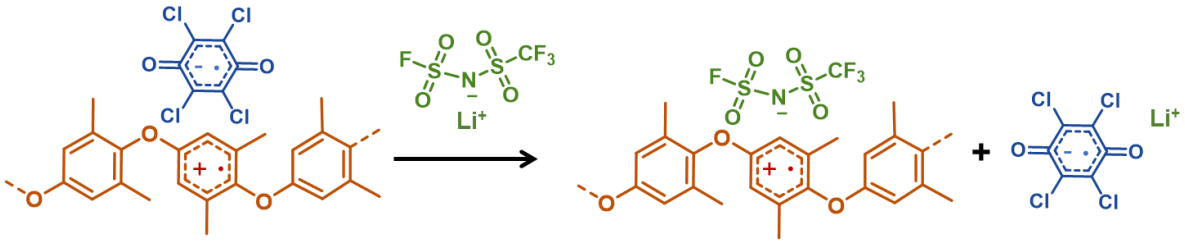


**Supplementary Figure 24 | Assumed anion exchange reaction induced by the addition of molten salts.**

**Supplementary Discussion g: Potential factors for conductivity**

As discussed in the main manuscript, ionic conduction was attributed to the amorphous phases of the salts. However, pristine salts displayed room temperature conductivities of around $10^{-10}$ S cm$^{-1}$. LiFTFSI became amorphous after heat treatment (Supplementary Figure 13b), even though it is practically an insulator as a pristine material (Figure 2c, LiFTFSI-HG). Additional components, represented by charge-transfer complexes, were essential for conductivity.

Apart from the polymer and donor molecules, the contribution of trace impurities, such as oxygen, water, and by-products from electrolyte formation, should be considered. Oxygen would help to dope polymers as an oxidant, although the effect would be negligible owing to the low oxygen concentration in the glove box (typically less than 10 ppm, Supplementary Figure 6). We did not detect substantial amounts of by-products with the characterization methods that we used.

Because trace amounts of water would increase the conductivity by acting as a solvent, we evaluated the water content in the electrolytes. Karl Fischer titration or the standard drying method was infeasible because of the acceptor molecules' redox capability and tendency to sublime. Therefore, the amount was estimated by $^{1}$H NMR (Supplementary Figure 25). After impedance, water was extracted from the electrolyte and measured by the following procedure. The electrolyte was put into deuterated dimethyl sulfoxide (DMSO-d6, 99.9% deuteration, Acros Co.). The concentration of the sample was 10 mg mL$^{-1}$ (= 0.0084 g per $g_{solvent}$). The insoluble components were filtered off; the PMPS electrolytes were mostly insoluble because of thermal cross-linking during electrolyte preparation. The water content in the solvent was measured by conventional solution $^{1}$H NMR.

In the absence of electrolytes, the relative proton peak area of water, initially contained in the solvent, was 0.85 compared with the normalized area of non-deuterated DMSO (Supplementary Figure 25a). By assuming a 99.9% deuteration ratio and solvent density of 1.19 g cm$^{-3}$, the water content was

converted by a coefficient of 0.0071 wt % per area, that is, the actual water content in the solvent was calculated as $0.85 \times 0.0071 = 0.006$ wt %.

The water content of the SLD67-56 electrolyte was estimated (Supplementary Figure 25b, c). The solid-state cells were kept in a glove box or under atmospheric conditions for 5 days, and the water peak areas were 0.78 and 0.63, respectively. The comparable values indicated that water contamination was not detectable by the current method.

This method's potential water sensitivity was estimated to be around $0.1 \times 0.0071 = 0.00071$ wt %, assuming significant digits of 0.1 for the peak area. The amount corresponds to 0.00071 wt % per $0.0084 \cong 0.1$ wt % of water in the original electrolyte, indicating that water was not the main matrix for conduction. In the future, more extensive structure analyses will be needed to explain the slight $^{7}$Li and $^{19}$F NMR peak shifts after the electrolyte formation and the high mobility of ions in the amorphous phases (Supplementary Figure 17 and Supplementary Figure 19).

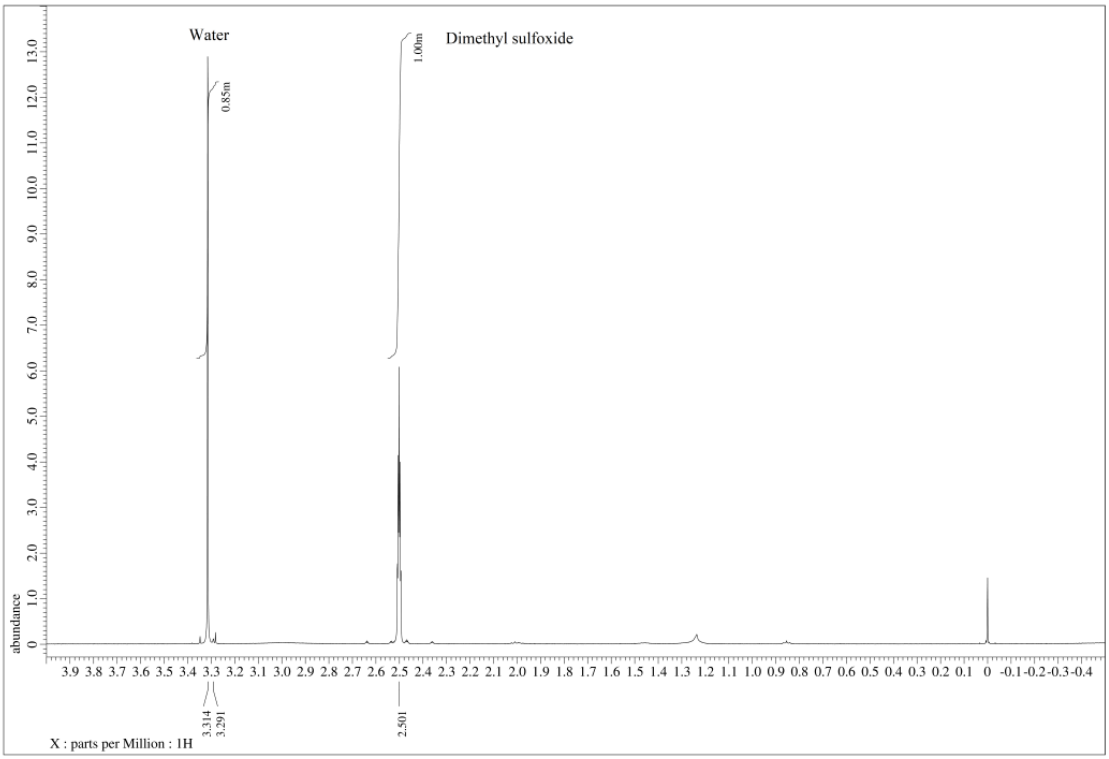
Water
Dimethyl sulfoxide
0.85m
1.00m
abundance
3.314
3.291
2.501
X : parts per Million : 1H

a)

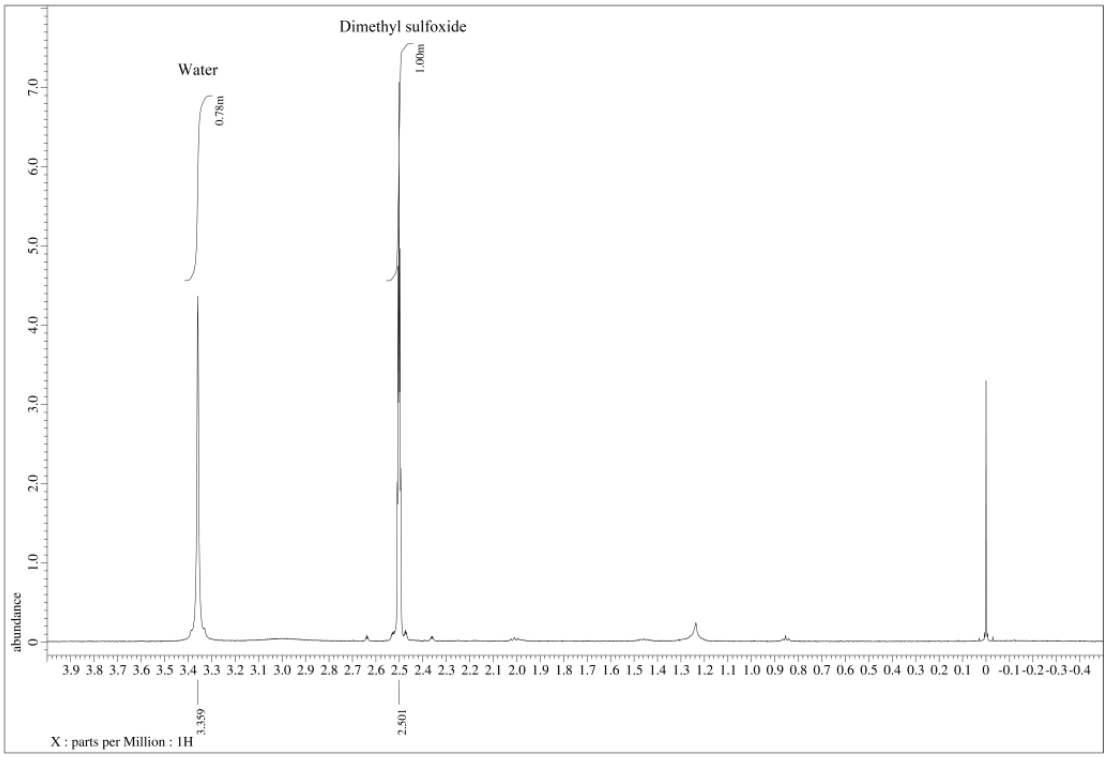
Dimethyl sulfoxide
Water
1.00m
0.78m
abundance
3.359
2.501
X : parts per Million : 1H

b)

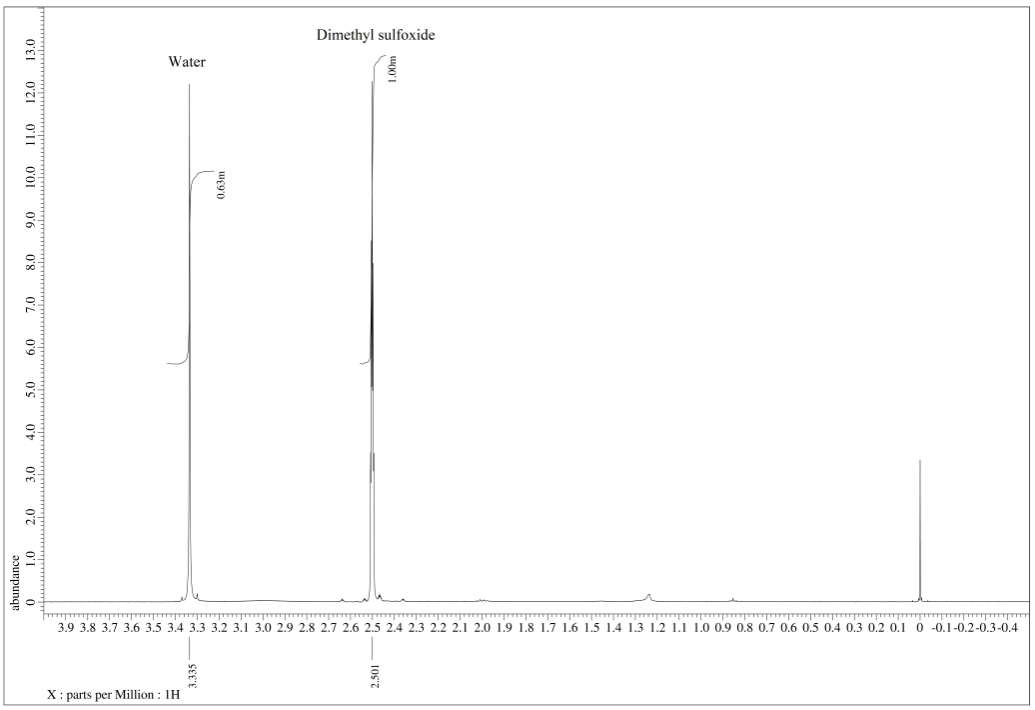
Dimethyl sulfoxide
Water
1.00m
0.63m
abundance
3.335
2.501
X : parts per Million : 1H

c)

**Supplementary Figure 25 | $^1$H NMR spectra of Deuterated DMSO containing electrolytes. a,** Pristine DMSO. **b,** DMSO containing the SLD67-56 electrolyte kept in a cell in a glove box. **c,** DMSO containing the SLD67-56 electrolyte kept in a solid-state cell in the air for 5 days.

**Supplementary Discussion h: Essential factors for conductivity and reproducibility**

The addition of charge-transfer complexes to lithium salts increased the room temperature ionic conductivity from around $10^{-10}$ to $10^{-8}-10^{-3}$ S cm$^{-1}$ (Figure 2c). However, the inhomogeneity of the electrolytes led to a large variation in conductivity of some electrolytes, even though they were prepared under the same experimental conditions. A modified score was defined as the median of $\sigma_{ion}$ minus the standard deviation of $\sigma_{ion}$ to discuss the reproducibility (Supplementary Figure 26a). A high score could be achieved only by an electrolyte displaying a high conductivity with sufficient reproducibility.

Similar to the standard $\sigma_{ion}$, the reproducibility score was predicted from the medians of explanatory variables (Supplementary Figure 26b). The $R^2$ values (around 0.5 for both training and testing) became smaller than for the standard case (over 0.8) because of the loss of sample-dependent information (e.g., thickness), but the value was high enough for the following SHAP value analysis

SHAP values indicated that the essential factor for conductivity and reproducibility was sufficient heating (Supplementary Figure 26c and d). Higher scores were observed when a specific heating process (typically, 300°C or 160°C for 30 min) and annealing before measurement were included. The heating was preferred, which induced appropriate molecular interactions among polymer, acceptor, and salt (e.g., LiFTFSI melts at around 110°C). A proper donor/acceptor/salt ratio was also critical to forming percolating pathways in the ion-conducting amorphous phase.

The SHAP analysis indicated the critical effects of component ratio to form conductive pathways in the electrolyte layers. In addition, the authors believe that the selection of molecules is essential. The lower molecular weight of the salt increased the conductivity; this corresponded mainly to using LiFTFSI instead of LiTFSI. The asymmetrical LiFTFSI molecule readily formed the amorphous phase. Similarly, PPO had much higher scores than PMPS (Supplementary Figure 26a). One technical reason could be the difficulty in mixing. Poly(phenylene sulfide) species underwent curing (cross-linking) reactions at high temperatures, which resulted in the formation of solid blocks of the materials.

In contrast, PPO, which is a viscous fluid at high temperatures, was easy to mix with acceptors and salts, enabling greater electrolyte homogeneity. There were no major differences between chloranil and benzoquinone as acceptors, but 2,3-dichloro-5,6-dicyano-*p*-benzoquinone yielded the lowest conductivity and produced a broad $^{7}$Li NMR spectrum (Supplementary Figure 17). Slight differences in molecular-level interactions with salts (e.g., Supplementary Figure 9), also affect the conductivity and reproducibility. We are currently conducting research into these molecular interactions.

According to the scores in Supplementary Figure 26a, one of the best electrolyte conditions was OLM60-41HG, which was a mixture of PPO/chloranil = 60/40 (mol/mol) with about 40 wt % LiFTFSI. The electrolyte was milled for over 150 min in total, which was also essential for achieving dense packing of the electrolyte particles. Actual room temperature ionic conductivity was as high as 0.3 to 0.8 mS cm-$^{1}$, whereas a non-optimized PMPS-chloranil-LiTFSI (SLD80-57LO) electrolyte suffered from an excessive variation of $\sigma_{ion}$ ($10^{-10}$ to $10^{-3}$ S cm$^{-1}$, Figure 2c).

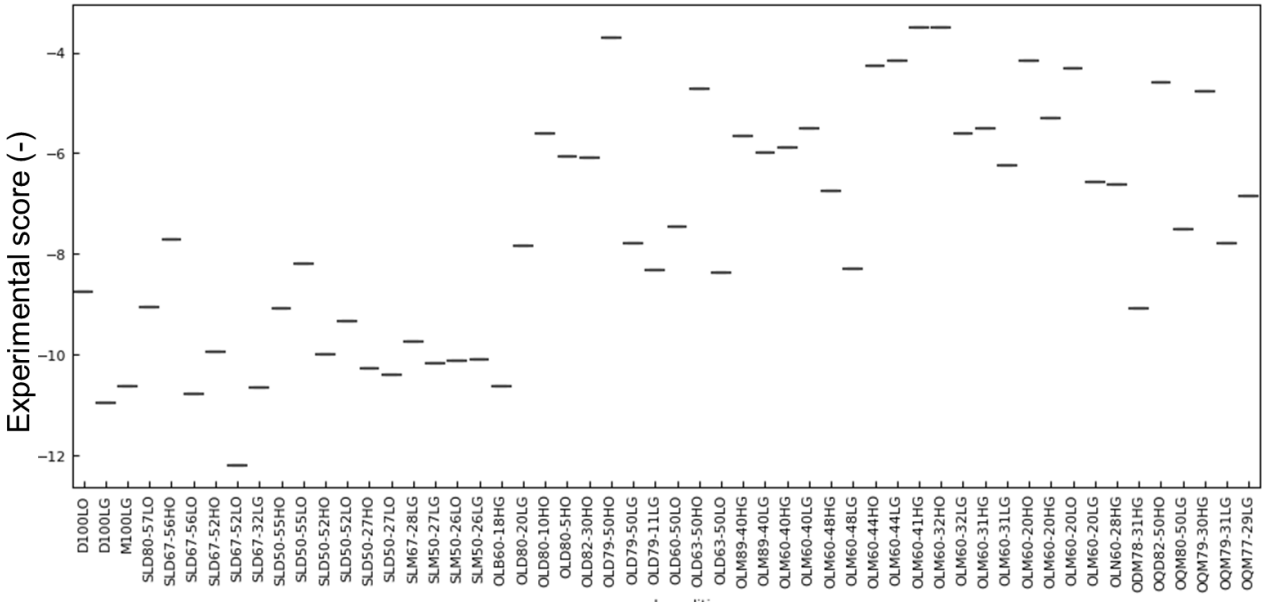
Experimental score (-)
−4
−6
−8
−10
−12
D100LO
D100LG
M100LG
SLD80-57LO
SLD67-56HO
SLD67-56LO
SLD67-52HO
SLD67-52LO
SLD67-32LG
SLD50-55HO
SLD50-55LO
SLD50-52HO
SLD50-52LO
SLD50-27HO
SLD50-27LO
SLM67-28LG
SLM50-27LG
SLM50-26LO
SLM50-26LG
OLB60-18HG
OLD80-20LG
OLD80-10HO
OLD80-5HO
OLD82-30HO
OLD79-50HO
OLD79-50LG
OLD79-11LG
OLD60-50LO
OLD63-50HO
OLD63-50LO
OLM89-40HG
OLM89-40LG
OLM60-40HG
OLM60-40LG
OLM60-48HG
OLM60-48LG
OLM60-44HO
OLM60-44LG
OLM60-41HG
OLM60-32HO
OLM60-32LG
OLM60-31HG
OLM60-31LG
OLM60-20HO
OLM60-20HG
OLM60-20LO
OLM60-20LG
OLN60-28HG
ODM78-31HG
OQD82-50HO
OQM80-50LG
OQM79-30HG
OQM79-31LG
OQM77-29LG

a)

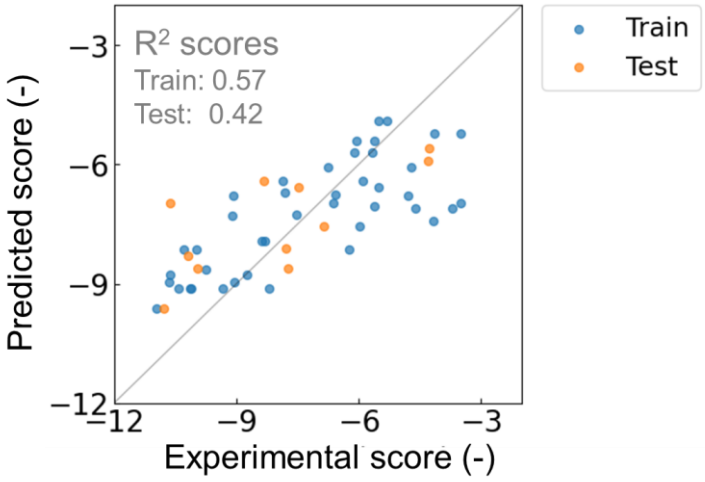
R² scores
Train: 0.57
Test: 0.42
Train
Test
Predicted score (-)
Experimental score (-)
−3
−6
−9
−12

b)

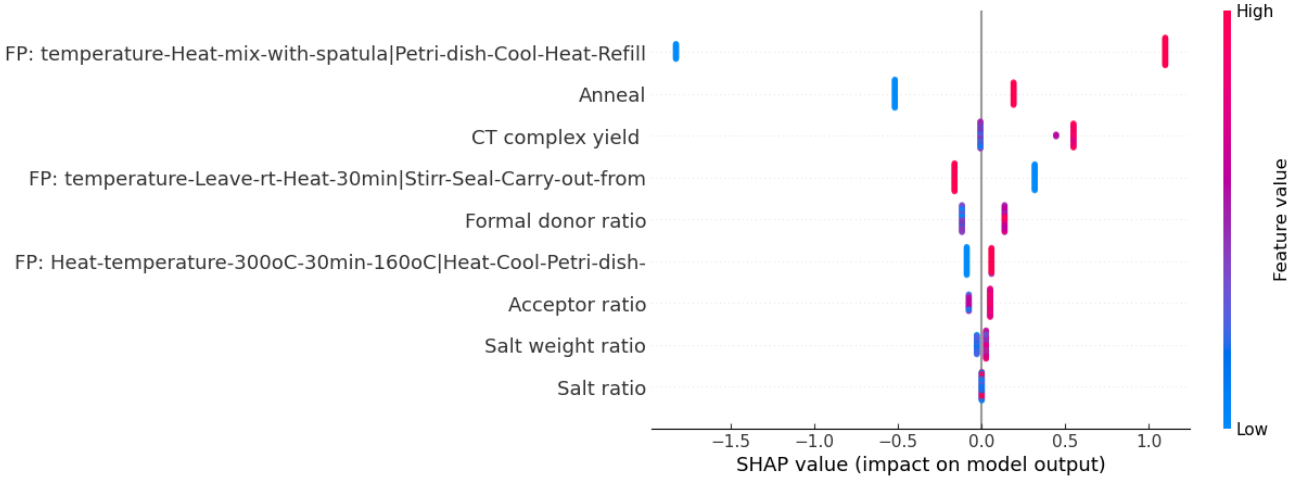
FP: temperature-Heat-mix-with-spatula|Petri-dish-Cool-Heat-Refill
Anneal
CT complex yield
FP: temperature-Leave-rt-Heat-30min|Stirr-Seal-Carry-out-from
Formal donor ratio
FP: Heat-temperature-300oC-30min-160oC|Heat-Cool-Petri-dish-
Acceptor ratio
Salt weight ratio
Salt ratio
−1.5
−1.0
−0.5
0.0
0.5
1.0
SHAP value (impact on model output)
High
Feature value
Low

c)

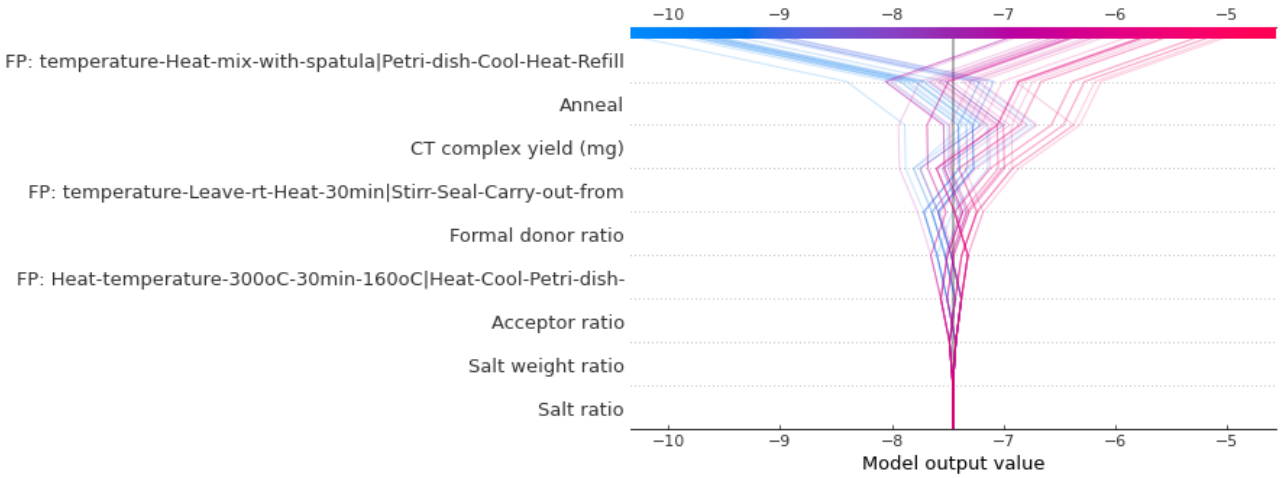


d)

**Supplementary Figure 26 | Prediction of conductivity scores instead of log $\sigma_{ion}$.** The scores were defined as the median of log $\sigma_{ion}$ minus its standard deviation. **a,** Scores for each electrolyte. **b,** Predicted and experimental values. **c,** SHAP values for the prediction model. **d,** Decision plot.

**Supplementary Discussion i: Battery analysis**

A lithium-ion battery with a $LiFePO_4$ cathode and a $Li_4Ti_5O_{12}$ anode was examined with a PPO/benzoquinone = 8/2 with 53 wt % LiFTFSI electrolyte. A redox wave was observed at $E_{1/2} \cong 1.9$ V, corresponding to the formal voltage (Supplementary Figure 27a). The areal discharging capacities were 0.34, 0.36, 0.35, and 0.27 mAh $cm^{-2}$ at 0.1, 0.2, 0.5, and 1 C, respectively, compared with the formal capacity of 1.5 mAh $cm^{-2}$ (1 C corresponded to a current of 1.18 mA, Supplementary Figure 27b). The experimental values were smaller than the theoretical value owing to the incomplete ionic conduction throughout electrodes; thus, the electrode fabrication should be optimized in future work.

The ohmic resistance of the cell, $R_{DC}$, was estimated by extracting the charging plateau voltages, defined as the values at 30% of the experimental charging capacities (Supplementary Figure 27c). From the slope, the resistance was estimated to be 270 Ω, which was used for the following transference number analysis.

After the rate tests, the cell was repeatedly charged/discharged at 0.05 C (Supplementary Figure 27d). The discharging capacity decreased gradually from 0.36 to 0.20 mAh $cm^{-2}$ over 30 cycles. The side reactions of the electrolyte and electrode caused this decrease. Further analysis is required to understand the capacity decrease and low Coulombic efficiencies (60%–95%) for practical applications.

Because the electrolytes were not highly stable to lithium, the $Li^+$ transference number was estimated from the battery results. The estimation was achieved by comparing the DC (charge/discharge) and AC (EIS) resistances of the electrolyte (Supplementary Figure 27e).

The ohmic resistance during the charge/discharge measurements, $R_{DC}$, should consist mainly of lithium migration resistance $R_{Li}$ and other battery resistances, such as electrode resistance, $R_{el}$ ($R_{DC} = R_{Li} + R_{el}$). The active carrier was only $Li^+$ during the charge/discharge of the lithium-ion battery. However, ionic conductivity resistance, $R_{ion}$, during the ESI measurement, consisted of both $Li^+$ and

anion resistances ($R_{ion}^{-1} = R_{Li}^{-1} + R_{anion}^{-1}$). According to the definition, $Li^+$ transference $t_{Li}$ is $\left(\frac{conductance\ of\ Li^+}{conductance\ of Li^+ + conductance\ of\ anion}\right) = \frac{1/R_{Li}}{1/R_{ion}} = \frac{1/(R_{DC}-R_{el})}{1/R_{ion}} = \frac{R_{ion}}{R_{DC}-R_{el}}$ (Supplementary Figure 27f).

The overvoltages of plateaus increased linearly along with the higher charging rates because of the ohmic resistance, $R_{DC}$, of the cell, which was estimated to be 270 Ω. At the same time, $R_{ion}$ was evaluated to be 211 Ω by impedance measurements. Therefore, the estimated transference number $t_{Li}$ was $270/(211 - R_{el}) = 0.78$ with $R_{el} = 0$. Considering $R_{el} > 0$, the actual $t_{Li}$ was more than 0.8.

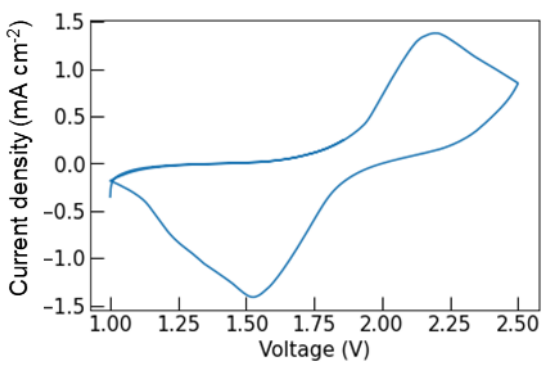


a)

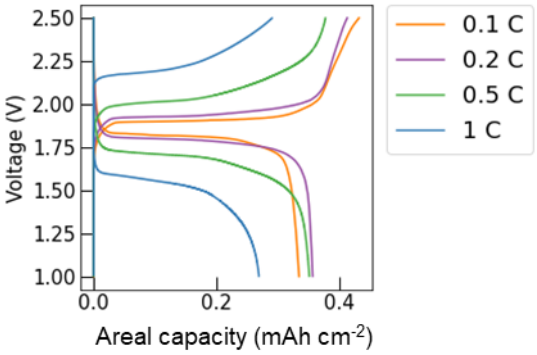


b)

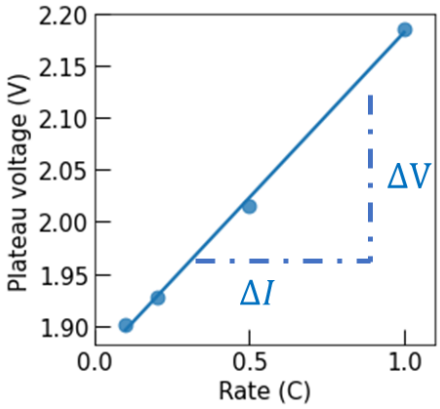


c)

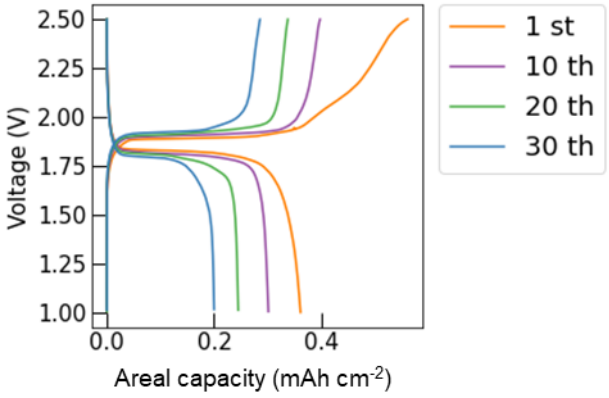


d)

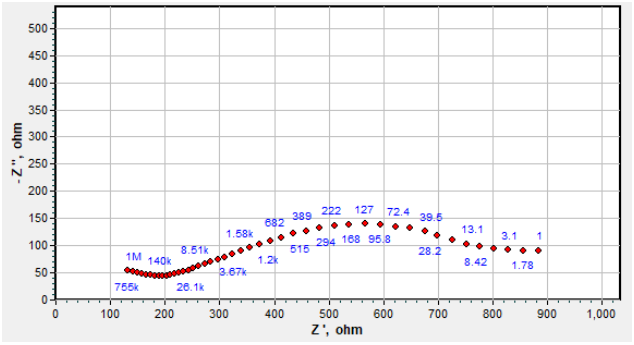


e)

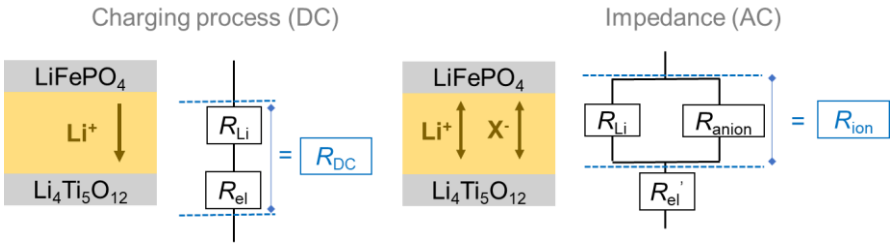


f)

**Supplementary Figure 27 | Properties of a prototype solid-state lithium-ion battery. a,** Cyclic voltammogram scanned at 0.5 mV $s^{-1}$. **b,** Charge/discharge curves at different rates. **c,** Plateau voltages during charging. Voltages at 30% of the experimental capacity were plotted. When applied current **$\Delta I$** increased, overvoltage $\Delta V$ increased according to Ohm's law ($\Delta V = \Delta I R_{DC}$). **d,** Charge/discharge curves at 0.05 C with different cycles. **e,** EIS spectrum of the cell after cycling. Blue captions show the measurement frequencies. The first partial semicircle was attributed to ionic conduction. **f,** Equivalent circuits for DC and AC measurements. Only lithium cations moved during the charge/discharge processes of the cell ($R_{anion} = \infty$). All electrochemical measurements were conducted at 50 °C.